2

Characterization of a Sub-Picosecond Dye Laser for the Study of Atom-Perturber Collisions

by

Scott Alan Fedorchak

B.S., United States Military Academy (1982)
M.S., Boston University (1985)

Submitted to the Department of Physics
in partial fulfillment of the requirements for the degree of

Master of Science in Physics

at the

MASSACHUSETTS INSTITUTE OF TECHNOLOGY

June 1991

Author ....Scott A Fedorchak....
Department of Physics
June 28, 1991

Certified by ....Ramachandra R Dasari....
Ramachandra R. Dasari
Principle Research Scientist
Thesis Supervisor

Certified by ....Michael S Feld....
Michael S. Feld
Professor of Physics
Thesis Supervisor

Accepted by ....
George F. Koster
Chairman, Departmental Committee on Graduate Students

DEPARTMENT OF THE ARMY
U.S. ARMY STUDENT DETACHMENT
MASSACHUSETTS INSTITUTE OF TECHNOLOGY
CAMBRIDGE, MASSACHUSETTS 02139

ATZI-TBD-S dist 29 June 1991

SUBJECT: Submission of Graduate Thesis for CPT Fedorchak, Scott A

MEMORANDUM FOR: Defense Technical Information Center, (ATTN: DTIC-FDAC), Building 5, Cameron Staion, Alexandria, VA 22304-6145

1. I have enclosed two copies of the completed graduate thesis, Characterization of a Sub-Picosecond Dye Laser for the Study of Atom-Perturber Collisions, prepared during the period 1 Sep 89 to 5 Jul 91 while I completed the requirements for the Master of Science Degree in Physics at the Massachusetts Institute of Technology, Cambridge, MA 02139 under the provisions of AR 621-1.

2. If you have any questions, please feel free to contact me at my current address:

CPT Scott A. Fedorchak

3. POC this memorandum is the undersigned at (914) 469-9623.

Ⓐ

Scott

2 Encl (as)

SCOTT A. FEDORCHAK
CPT, MP
184-52-2508

Characterization of a Sub-Picosecond Dye Laser for the Study of Atom-Perturber Collisions

by

Scott Alan Fedorchak

Submitted to the Department of Physics
on June 28, 1991, in partial fulfillment of the
requirements for the degree of
Master of Science in Physics

Abstract

This thesis covers an in-depth analysis of the pulsed laser system to be used in developing a linear technique for the time domain study of the change in coherence of atomic superposition states for the Ytterbium atom due to phase-interrupting collisions. The hybrid synchronously pumped dye laser yielded optimally shaped sub-picosecond pulses at the 555.6 nanometer wavelength. Comparison of the results for the experimental trials at the 576 and 555.6 nanometer wavelengths yielded an experimental value for the dephasing time, $T_2 = 621$ picoseconds, of the DMETCI dye used as a saturable absorber dye for the first time.

Thesis Supervisor: Ramchandra R. Dasari
Title: Principle Research Scientist

Thesis Supervisor: Michael S. Feld
Title: Professor of Physics

Acknowledgments

I would like to thank Dr. Michael Feld and Dr. Ramchandra Dasari for giving me the opportunity to work and learn in the George Harrison Spectroscopy Laboratory as well as standing by me when problems developed. Additionally, the Spectroscopy Laboratory members, in particular Joe Baraga, Mark Doxtader and Gary Hayes and the rest of the gang deserve my thanks for their help and the hours spent in conversation over physics, laser spectroscopy and various regional and political issues.

I would like to extend a very special thank you to Kyungwon An who made everything happen when I could not get the equipment to work or was totally lost. He spent long hours explaining the theoretical and experimental procedures of the experiment in the office and laboratory, not to mention the many hours of hands-on work. This thesis would not have been possible without his tireless work, direction and assistance.

I would also like to thank Jim Childs and Mike Otteson for their guidance and help in repairing my laser systems when they broke.

I would also like to thank Matt Banet and Lisa Dhar of the Chemistry Department for their help in getting the Antares 76-S Laser up and running with the new high power second harmonic generator and helping me in keeping it that way.

Mark LeClerc from Coherent, Inc. deserves my thanks for the many hours we spent fixing the Antares together.

CPT Vernon Davis deserves special thanks for his help in getting me through the first year of graduate school here at MIT and for allowing me to trounce him repeatedly in extended EMPIRE competition. Likewise, MAJ Joseph Mackin, LTC Thomas Lainus and CPT Tim Creamer get my thanks for hours spent in reminding me why I put myself through this and helping me to continue to think "green."

Last and most importantly, I would like to give a very special thank you for my fiancee, Krista Fairbanks, by being there for me when I needed it. I promise you that we will have better times together as we plan our future together.

Contents

List of Figures

List of Tables

Chapter 1

Introduction

This thesis explores the pulse characteristics of the hybrid synchronous pumped dye laser for use in the study of the change of coherence of the atomic superposition states for the Ytterbrium atom due to phase-interrupting collisions. The detail of the phase-interrupting collisions requires a sub-picosecond pulse.

1.1 General overview

Collisional processes between atoms have been studied in some detail by different scientific fields since the phenonema was first postulated by Michelson in 1885 [Michelson1885]. The advance of scientific techniques and technology, notably laser spectroscopy, has greatly increased our understanding of the processes involved in collisional phenonema. From the early days of macroscopic observation of collisional processes through the classical and now quantum mechanical treatment of the behavior, physicists have expanded our levels of knowledge of the collisional processes. The development of lasers and laser spectroscopy has both facilitated and encouraged the study of collisional processes by providing a probe mechanism that can probe the sample and collect data on the collisions with minimal disruption of the process. The most commonly used technique involved in studying collisional processes using laser spectroscopy involve the use of atomic or molecular vapor in an enclosed sample cell. Researchers select the appropriate laser wavelength that excites the sample system to a excited state then study the resultant re-radiation of emitted light as the sample decays back to the ground state. When analyzed, the resultant spectra yields information on collisional processes. The most common technique to reduce the mean time between collisions is to introduce an inert buffer gas as a perturber atom into the sample cell that does not absorb laser light at the required wavelength.

Recent work has been focussed on the study of the polarization decay by collisional processes of the emitted light. The theoretical framework has been established by V.N. Rebane [Rebane1967] and its applications in the study of other collisional related phenomena has been used by several other researchers [Ghosh et al1984] [Pinard1979] [Hansch1969] [Le Gouet1980]. The initial work in the field on studying phase-interrupting collisions was done in the frequency domain; which through the appropriate Laplacian transforms, can be transformed into time domain information. A direct study of the collisional processes in the time domain can provide more direct yields of information on the phenonema. The photon echo technique using cw lasers applied to study collisional processes [Forber1983] was one of the first techniques to study these processes in the time domain. This non-linear technique provided invaluable information yet suffered from complications in analysis as users must ensure that the AC Stark effect does not induce modifications to the collisional processes. A more simplified linear approach was then devised to eliminate possible AC Stark effect interference with collisional processes. The linear technique developed by K. An et al [An et al 1988] uses a low power laser with ultra-short pulses to study collisional processes in the impact and quasi-static regime. This process involves directing two ultra-short laser pulses into a radiator-perturber system. The two pulses are created by sending the pulsed laser output into a beam splitter and directing one of the beams along a variable delay line, then re-directing the delayed pulse along the same path as the initial pulse, thereby allowing a controllable delay time between the two pulses. The first pulse, with its established and well-defined phase, excites the simple two level radiator atoms into an excited superposition state. This superposition state has an initially established phase that evolves in time. The second pulse, which has its own well-defined phase, will interfere with the macroscopic polarization of the system

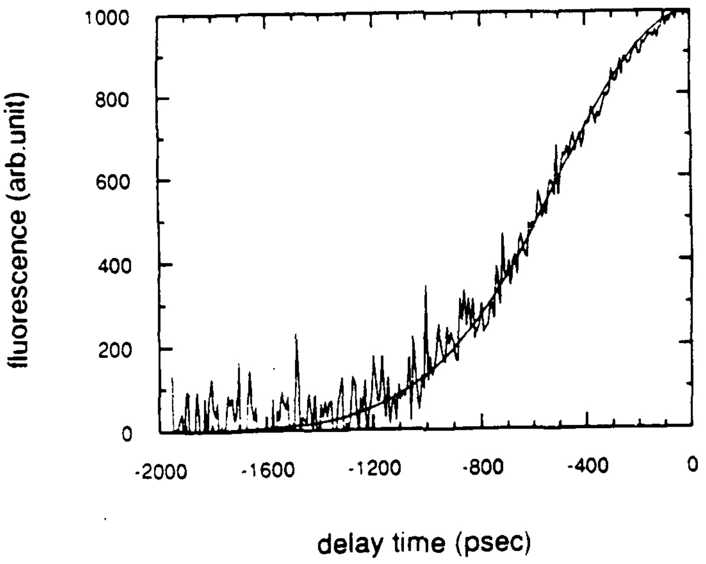

Figure 1-1: Picosecond Time Domain Study of Atomic Superposition State Collisions [An et al 1988]

reflected by the modulation of the excited upper state population. If there are no dephasing mechanisms such as collisions, the coherence of the macroscopic polarization will not decay within twice of the spontaneous lifetime of the excited state for the two level atom. By monitoring the fluorescence of the system, we can measure the degradation of the macroscopic polarization coherence caused by the collisions. This will show up in the form of a decrease in the fluorescence signal as the delay time between successive pulses increases. By varying the number of radiator-perturber atoms in the system, we can alter the mean time between collisions and gain further information on the collisional processes. Typical perturber atoms used in the experiment are inert buffer gases such as Helium, Argon or Xenon.

The initial experimental results for this linear technique were conducted in 1988 using a picosecond regime pulsed laser. ^{174}Ytterbrium was used as the two-level radiator atom for the phase-interrupting collision experiment. Experimental results are shown in figures 1.1 and 1-2 on pages 11 and 12. The $x-axis$ of the figures represents the delay time between successive pulses, τ_d while the $y-axis$ depicts the recorded fluorescence signal in arbitrary units. The data in figure 1.1 was taken with

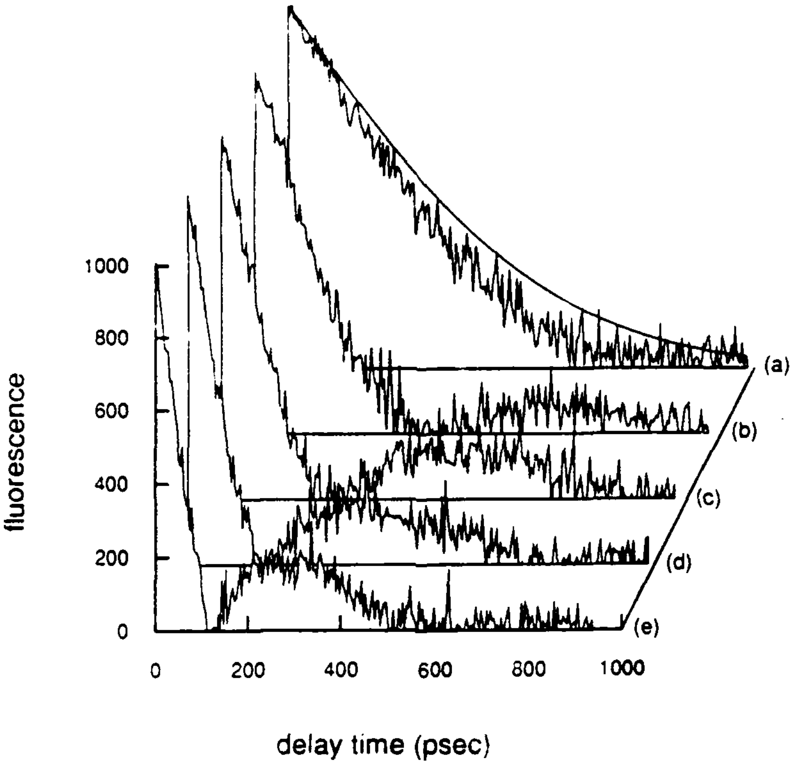

Figure 1-2: Picosecond Time Domain Study of Atomic Superposition State Collisions with Argon Buffer Gas [An et al 1988]

the Ytterbrium concentration at 2.2×10^{11} cm^{-3} and without a buffer gas.

The data in figure 1-2 was run at differing Ytterbrium vapor concentrations; (a) 2.5×10^{10} cm^{-3}, (b) 1.0×10^{11} cm^{-3}, (c) 2.1×10^{11} cm^{-3}, (d)3.4×10^{11} cm^{-3}, and (e) 7.0×10^{11} cm^{-3}, with the Argon buffer gas concentration set at 9.0×10^{17} cm^{-3} to explore collisional behavior as the mean time between collisions was decreased. Note that the presence of the buffer gas smoothens out the spikes in the original figure 1.1.

The decay curves show a gaussian curve associated with a Doppler dephasing. There is a significant amount of agreement with the predicted smooth curve that is the product of a gaussian curve with Doppler dephasing and an exponential curve with Doppler dephasing. There is also the presence of possible peaks or other details at the higher density regimes which are caused by non-linear effects of the higher sample concentrations that cannot be clearly discerned from the background noise. Figure 1-3 on page 13 depicts a comparison of the data taken in R. Forber's photon echo technique for ^{174}Yb (shown as the horizontal line with 10 percent error bars) [Forber1983] versus the data taken using the linear technique developed by K. An (shown as the o with error bars) [An et al1988]. The figure depicts the decay rate of

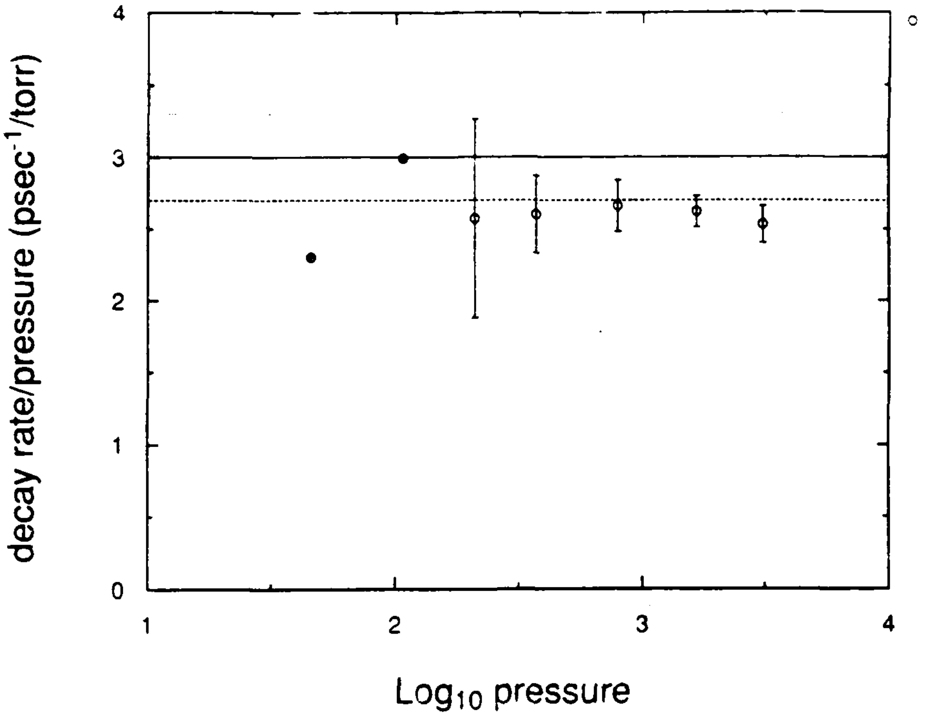

Figure 1-3: Comparison of data by photon echo [Forber1983] with data by linear technique [An et al1988]

Ytterbium in units of $\frac{psec^{-1}}{torr}$ on the $y-axis$ as a function of the pressure in units of log_{10} $torr$ on the $x-axis$. The two techniques show an agreement with each other with the linear technique showing more detail of the collisional structure.

The laser used to take this data produced a pulse width on the order of 5 picoseconds and is shown in figure 1-4 on page 14 with the half pulse intensity profile depicted as the lower data curve and the resulting decay curve depicted as the upper curve.

This figure clearly shows the presence of the broad incoherent background associated with this laser pulse and the corresponding peaks in the decay curve caused by the wings of the pulse. The average output power of this system was on the order of four milliwatts.

The use of this picosecond regime laser pulse potentially obscured some of the details of the collisions by not allowing sufficient resolution of detail. The duration of the collisions between Ytterbrium and the perturber atoms can be estimated by calculating the radius of the ^{174}Yb atom's outermost electron and calculating the

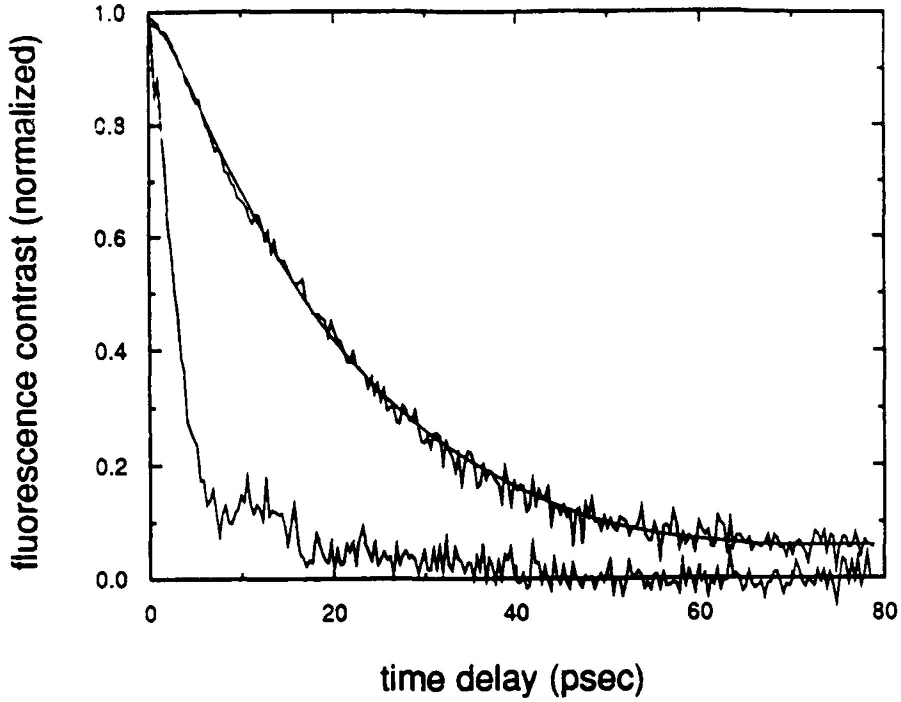

Figure 1-4: Laser Pulse used in Study of Phase Interrupting Collisions [An et al1988]

velocity if the atom by

$$v = \sqrt{\frac{2k_BT}{m}} \tag{1.1}$$

Dividing the atomic diameter by the atom's velocity yields a collision duration on the order of 3 picoseconds. To approach the quasi-static collision limit in the study of these collisions, we must have $t_{pulse} \ll t_{coll}$. The use of sub-picosecond pulses should allow the resolution of the finer details of the phase-interrupting collisions.

1.2 Ytterbrium Atom

The radiator atom used in the study of phase-interrupting collisions should be as simple as possible to minimize multi-level degeneracy and collisional coupling effects and transitions and to facilitate the analysis of the results. The two level atom should have an allowed transition within the spectral range of available chemical dye lasers; and the temperature at which the atomic vapor is formed should be relatively low to facilitate the atom vapor production. [Forber1983][Ghosh et al1984] Additionally, the atom should have a simplified atomic structure with a $^1S_0$ ground state, no net spin, and other allowed transitions sufficiently distanced to preclude excitation to other allowed transitions. ^{174}Ytterbrium was selected for its characteristics which virtually optimized the above criteria. ^{174}Ytterbrium is a simple two-level system with an allowed $^1S_0$ to $^3P_1$ dipole transition at 555.6 nanometers wavelength energy separation. This atom's nuclear spin of the ground state is zero with no hyperfine structure. The closest fine-structure energy level is 700 cm^{-1} away which minimizes the possibility of exciting other allowed transitions. The spontaneous lifetime, t_{spon}, is relatively long, 895 nanoseconds [Corliss1962], which allows us to approach the quasi-static limit with sufficiently short laser pulses. With the t_{spon} much larger than the duration of the collisions, τ_{coll}, and τ_{coll} much larger than the laser pulsewidth, we can approach the impact collision limit and gain invaluable information on the dynamic aspects of the collision. The temperature for low pressure atomic vapor (10^{-6} torr) is 352 degrees Celsius [Nesmeyanov1963], which allows for easy formation of Ytterbrium metal vapors using Inconnel 600 heating elements on the sample cell. The 555.6 nanometer wavelength corresponding to the desired transition is within the spectral range of commercially available dye lasers.

1.3 Laser System Requirements

The selection of the Ytterbrium atom dictates the wavelength of the required laser output and subsequent laser system requirements. To allow study of the collisional processes at the quasi-static collision limit, the laser's pulsewidth, or τ_{pulse} must be much smaller than the duration of the collisions, τ_{coll}. Therefore, we should have the τ_{pulse} on the order of a few hundred femtoseconds to allow maximum detail of the collisional processes to be viewed. Optimal pulseshape, to include the elimination of satellite pulses and wings to the pulse, should be maintained to limit the induced macroscopic polarization of the Ytterbrium sample to the initial pump pulse. Any satellite pulses or irregularly shaped pump pulses could cause additional superposition states with differing polarization phases that interfere with the initial polarization and cause unnecessary complications to the data analysis.

During preliminary trial runs of the experiment to test the equipment with the cavity dumper in the laser system and an external pulse compression apparatus to

Laser System	Mode-Locking Technique	Laser Components	Average Pulse
Passive	Saturable Absorber	Nd:YAG/Dye	1 ps
Synchronous Pumping	Modelocked Pump Laser with Saturable Absorber	Dye	5 ps
Hybrid Synchronous Pumping	Same as Sync. Pumping except Separate Saturable Absorber Jet	Dye	500 fs
Ring Cavity (CPM)	Passive Modelocking in Ring Cavity	Dye	100 fs

Table 1.1: Mode-Locking Techniques for Short Laser Pulses

decrease the pulsewidth to the sub-picosecond regime , losses through the optics and diagnostic equipment of the experiment reduced the output power from the dye laser from 4 milliwatts at the output coupler to 7 microwatts at the entrance to the sample cell window. This initial power level did not stimulate sufficient Ytterbrium atoms to the superposition state to allow sufficient fluorescence to discern collisional data from background noise. Since losses from the experimental setup could only be marginally reduced through narrow band anti-reflective coating of the optics, the output power of the laser must be increased by at least a factor of 10 in order to gain sufficient fluorescence to produce meaningful experimental results.

There are a variety of laser systems available to produce ultra-short laser pulses. The majority of these mode-locking techniques use a variety of mechanisms to shape and control the pulse. Common techniques used for laser short pulse generation are shown in table 1.1 on page 16. Another external method not listed in this table to shorten the pulsewidth is to build an external pulse compression apparatus and place the pulse laser output through the device. This thesis covers theoretical and initial work in this area as a possible option for use in the experiment.

Of the mode-locking techniques listed in table 1.1, only three techniques, synchronous pumping, hybrid synchronous pumping and and colliding pulse modelocking (CPM), produce pulsewidths in the time regime that is required. Synchronous pumped and hybrid synchronous pumped lasers differ only in the fact that the synchronous pumped laser combine the dye and saturable absorber dyes in a single jet while the hybrid system uses a separate saturable absorber jet to acheive an order of magnitude smaller pulsewidth. The hybrid synchronous pumped laser is the only sub-picosecond regime laser that gives us the tunability through the desired ^{174}Ytterbrium wavelength.

Although the CPM or ring cavity laser system produces the shortest pulsewidth on record, it suffers from low power and minimal tunability.

Based on these criteria for the phase-interrupting collision experiment, the hybrid synchronously pumped dye laser was selected as having the optimal characteristics to meet these standards for the experiment.

1.4 Thesis Organization

This thesis is organized into eight chapters. The first five chapters present general background, theoretical framework, equipment and the setup and operation of the equipment and experiment. The next two chapters cover the experimental results at the 576 nanometer and 556 nanometer wavelengths. The final chapter covers the analysis of the data, conclusions and recommendations.

Chapter 1 covers a general outline of the linear technique used in studying the superposition states, the selection and description of the Ytterbrium atom, an outline of laser system requirements to be used and the overall context of the experiment.

Chapter 2 covers the theory of the atomic two level systems, collisional theory, and phase-interrupting collisions and sets the theoretical requirements for the laser system.

Chapter 3 covers the theory of hybrid synchronously pumped dye lasers along with sections on saturable absorber theory and pulse compression techniques.

Chapter 4 covers the equipment and chemical dyes used , physical setup of the experiment and description of the preliminary actions and procedures used prior to the data taking process during the experiment.

Chapter 5 covers the actual conduct of the experiment with the procedures used for data acquisition and initial trial results for the hybrid synchronously pumped laser operating at its peak efficiency.

Chapter 6 covers the data taken during the experiment at the 576 nanometer wavelength and initial analysis of the results.

Chapter 7 covers the data taken at the required 556 nanometer wavelength with the initial analyis and discussion.

Chapter 8 covers the final analysis of the experimental data, the conclusions and recommendations for areas of future experimentation.

Chapter 2

Phase Interrupting Collisions

This chapter covers the theory of the two level atom that Ytterbrium^{174} displays from the basic theory though the phase interrupting collisional processes to demonstrate the requirements for the pulsed laser output. The theory for the phase-interrupting collision experiment was developed by Kyungwon An and is covered in brief in this chapter. The extended mathematical derivations for formulas will not be explicitly shown in every detail; pertinent steps of the derivations will be shown along with the supporting references and documentation for further information.

2.1 Two Level Systems

The ^{174}Ytterbrium atom used in the experiment is a simple two level atom with an allowed $^1S_0$ to $^3P_1$ transition. As stated before, the linear technique used for the phase-interrupting collision experiment uses two laser pulses to excite and probe the radiator-perturber system. The first pulse of the incident laser radiation excites the Ytterbrium atom to the upper level, creating a two level system with a separation of $\hbar\omega$ as shown in figure 2-1 on page 20.

If left unperturbed, this two level ^{174}Ytterbrium system will decay with a lifetime, t_{spon}, equal to 875 nanoseconds. We can write the equation of motion for the system as

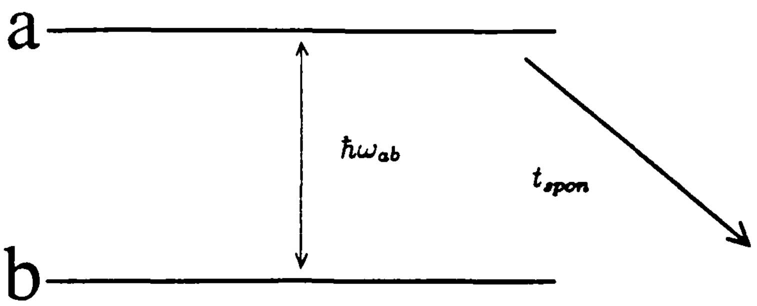

Figure 2-1: Two Level Unperturbed System

$$i\hbar\frac{\partial\rho}{\partial t} = [H_{tot}, \rho] \tag{2.1}$$

where H_{tot} is the total Hamiltonian for the system given by

$$H_{tot} = H_O + U \tag{2.2}$$

where H_O is the original Hamiltonian of the system and U is the electric dipole matrix interaction. If we assume operation near resonance of the system, we can use the rotating wave approximation and neglect the high frequency oscillations of the system. We can then write the matrix element, U_{ab}, of the off-diagonal 2 x 2 matrix U as

$$U_{ab} = -\vec{\mu_{ab}} \cdot \vec{E(t)}\frac{1}{2}e^{-i\Omega t} \tag{2.3}$$

When $U_{ab} = U^*_{ba}$, and $U_{aa} = U_{bb} = 0$, the electric dipole matrix term, μ_{ab}, corresponds to the transition rate, $\dot{\rho}_{ab}$, between the excited state, Level A, and the ground state, Level B, as depicted in figure 2-1 shown on page 20 [Feld1977].

The key transition rates in this study of phase-interrupting collisional processes are $\dot{\rho}_{aa}$ and $\dot{\rho}_{ab}$ which correspond to the upper level of the system because we are looking for the effects of collisions on the coherence of the superposition states of the Ytterbrium atom. These transition rates are defined by the following equations

$$\dot{\rho}_{ab} = -i\omega_0\rho_{ab} - \frac{i}{2}\chi(t)e^{-i\Omega t}\rho_D - \frac{\gamma_a}{2}\rho_{ab} \tag{2.4}$$

and

$$\dot{\rho}_{aa} = -\gamma_a\rho_{aa} + \frac{i}{2}\chi(t)e^{-i\Omega t}\rho_{ba} + -\frac{i}{2}\chi(t)e^{i\Omega t}\rho_{ab} \tag{2.5}$$

where $\chi(t)$ is the Rabi frequency of the system, $\gamma_a = \frac{\Gamma_{sp}}{2}$ corresponding to the spontaneous lifetime of the two-level system and ρ_D corresponds to the population inversion of the system sample. Their forms are given by the following equations

$$\chi(t) = \frac{\vec{\mu_{ab}} \cdot \vec{E(t)}}{\hbar} \tag{2.6}$$

and

$$\rho_D = \rho_{aa} - \rho_{bb} \tag{2.7}$$

2.2 Two Level Systems in Collisions

If the original excited state system collides with a perturber atom while in the excited state, the original atom will receive an incremental increase in energy equal to $\hbar\delta\omega(t)$ as shown in figure 2-2 on page 22.

Now the total Hamiltonian is written with the non-zero term, V, for the increase in potential energy due to collision.

$$H_{tot} = H_0 + U + V \tag{2.8}$$

where V is the perturbation due to collision. If we assume that the collision induces an energy shift in the system and not inducing a transition, we can write V as a diagonalized 2 x 2 matrix showing the energy shift due to collision where the

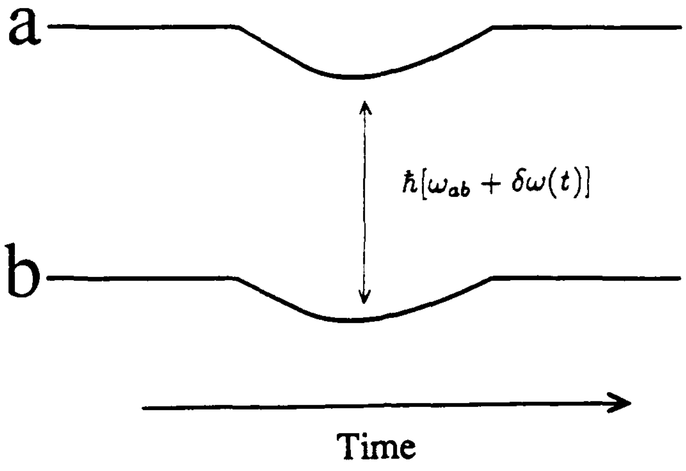

Figure 2-2: Two Level System Undergoing Collision

cross terms, V_{aa} and V_{bb} are given by

$$\hbar\delta\omega(t) = V_{aa}(t) - V_{bb}(t) \tag{2.9}$$

Equation 2.4 can be rewritten as

$$\dot{\rho}_{ab} = -i[\omega_0 + \delta\omega(t)]\rho_{ab} - \frac{i}{2}\chi(t)e^{-i\Omega t}\rho_D - \frac{\gamma_a}{2}\rho_{ab} \tag{2.10}$$

showing the incremental energy shift of equation 2.9 due to collisions. All other terms remain defined the same as they were in section 2.1 above.

To show the effects of this incremental increase, the ρ's can be expanded in terms of a perturbation expansion where the non-zero terms are

$$\rho_{aa} = \rho_{aa}^{(0)} + \rho_{aa}^{(2)} + \rho_{aa}^{(4)} + \ldots \tag{2.11}$$

and likewise for ρ_{ab},

$$\rho_{ab} = \rho_{ab}^{(1)} + \rho_{ab}^{(3)} + \rho_{ab}^{(5)} + \ldots \tag{2.12}$$

We define

$$\rho_D^{(0)} = \rho_{aa}^{(0)} - \rho_{bb}^{(0)} \tag{2.13}$$

as the initial population inversion of the sample and start the first order perturbation for ρ_{ab} as

$$\rho_{ab}^{(1)}(t) = \tilde{\rho}_{ab}^{(1)} e^{-i[\phi(t)+\omega_0 t]} e^{-\frac{\gamma_a t}{2}} \tag{2.14}$$

which gives

$$\dot{\tilde{\rho}}_{ab}^{(1)} = -\frac{i}{2}\chi(t) e^{-i\Omega t} e^{i(\phi+\omega_0 t)} e^{\frac{\gamma_a t}{2}} \rho_D^0 + C.C. \tag{2.15}$$

where $\phi(t)$ is the integrated phase shift of the $\delta\omega$'s of the excited state population. Using the definition for $\rho_D^{(0)}$ and defining $\Delta = \Omega - \omega_0$ as the detuning, this becomes

$$\dot{\tilde{\rho}}_{ab}^{(1)} = -\frac{i}{2}\chi(t) e^{-i(\Delta t-\phi)} e^{\frac{\gamma_a t}{2}} \rho_D^{(0)} \tag{2.16}$$

Integrating this equation yields

$$\tilde{\rho}_{ab}^{(1)} = -\frac{i}{2}\rho_D^{(0)} \int_{-\infty}^{t} dt' \chi(t') e^{-i[\Delta t' - \phi(t')]} e^{\frac{\gamma_a t'}{2}} \tag{2.17}$$

In a similar manner, $\rho_{aa}^{(2)}$ becomes

$$\rho_{aa}^{(2)}(t) = \tilde{\rho}_{aa}^{(2)} e^{-\gamma_a t} \tag{2.18}$$

Continuing the perturbation for $\rho_{aa}^{(2)}$, we get

$$\dot{\tilde{\rho}}_{aa}^{(2)} = \frac{i}{2}\chi(t) e^{-i\Omega t} e^{\gamma_b t} e^{i(\phi+\omega_0 t)} e^{-\frac{\gamma_a t}{2}} \tilde{\rho}_{ba}^{(1)} + C.C. \tag{2.19}$$

Using the complex conjugate of equation 2.17 for $\rho_{ba}^{(1)}$ and integrating equation 2.19, we get

$$\dot{\tilde{\rho}}_{aa}^{(2)} = (\frac{-\rho_D^{(0)}}{4}) \chi(t) e^{-i[\Delta t - \phi t]} e^{\frac{\gamma_a t}{2}} \int_{-\infty}^{t} dt' \chi^*(t') e^{i[\Delta t' - \phi(t')]} e^{\frac{\gamma_a t'}{2}} \tag{2.20}$$

where$\Delta = \Omega - \omega_0$ is the detuning. Equation 2.20 yields

$$\rho_{aa}^{(2)}(t) = (\frac{-\rho_D^{(0)}}{4})e^{-\gamma_a t}[\int_{-\infty}^{t} dt'\chi(t')e^{-i[\Delta t' - \phi(t')]}e^{\frac{\gamma_a t'}{2}} \int_{-\infty}^{t'} dt''\chi^*(t'')e^{i[\Delta t'' - \phi(t'')]}e^{\frac{\gamma_a t''}{2}} + C.C.] \tag{2.21}$$

where

$$\phi(t) = \int_{-\infty}^{t} dt'\delta\omega(t') \tag{2.22}$$

If we consider the time-averaged ensemble of equation 2.21 over a period of time, T, which is much longer than other relative time scales, we can define the ensemble by the following equation.

$$\langle\rho_{aa}^{(2)}(t)\rangle_T \equiv \frac{1}{T}\int_{-\frac{T}{2}}^{\frac{T}{2}} dt\rho_{aa}^{(2)}(t) \tag{2.23}$$

Defining that portion of equation 2.21 inside the integrand as simply a function of time, $F(t)$, and integrating by parts, we get

$$\langle\rho_{aa}^{(2)}(t)\rangle_T = \frac{1}{T}[\frac{e^{-\gamma_a t}}{-\gamma_a}F(t)]\,|_{-\frac{T}{2}}^{\frac{T}{2}} + \frac{1}{T\gamma_a}\int_{-\frac{T}{2}}^{\frac{T}{2}} e^{-\gamma_a t}F'(t) \tag{2.24}$$

If we assume that $F(\frac{T}{2}) = 0 = F(-\frac{T}{2})$ which implies that there is no significant steady state population in the excited state, the first term in equation 2.24 is negligible and can ignored, yielding

$$\langle\rho_{aa}^{(2)}(t)\rangle_T = \frac{1}{T\gamma_a}\int_{-\frac{T}{2}}^{\frac{T}{2}} e^{-\gamma_a t}F'(t) \tag{2.25}$$

Taking the derivative of $F(t)$ as defined above, re-arranging terms and using the change of variables $t'' - t' = \tau$ and then doing some further algebraic manipulation of equation 2.25 yields

$$\langle \rho_{aa}^{(2)} \rangle_T = (\frac{-\rho_D^{(0)}}{4})(\frac{1}{\gamma_a T}) \int_{-\infty}^{\infty} d\tau e^{-\frac{\gamma_a|\tau|}{2}} e^{i\Delta\tau} \int_{-\frac{T}{2}}^{\frac{T}{2}} dt_1 \chi(t_1)\chi^*(t_1+\tau) e^{-i\int_{t_1}^{t_1+\tau} dt'\delta\omega(t')} \tag{2.26}$$

The above derivation covers the process of two atoms colliding in the sample cell. Now we can consider the statistical aspects of $\mathcal{N}$ perturber atoms colliding in the sample cell, rewriting this equation over the n such collisions as

$$\langle \rho_{aa}^{(2)} \rangle_{time} = \frac{1}{\mathcal{N}} \sum_{n=1}^{\mathcal{N}} \langle \rho_{aa}^{(2)} \rangle \tag{2.27}$$

In evaluating equation 2.26, only the last exponential integral deals with the single atom and time periods T, t_1, and τ. Working solely within the exponential $e^{i[\int_{t_1}^{t_1+\tau} dt'\delta\omega(t')]}$ and defining everything to the left of this exponential as the function, $\mathcal{G}$, equations 2.26 and 2.27 can be combined to form

$$\langle \rho_{aa}^{(2)} \rangle_{time} = \mathcal{G} \frac{1}{\mathcal{N}} \sum_n exp[i \int_{nT+t_1}^{nT+t_1+\tau} dt'\delta\omega(t')] \tag{2.28}$$

By using the Ergodic theorem where the time average is equal to the ensemble average, we can reduce this equation to

$$\langle \rho_{aa}^{(2)} \rangle_{time} = \mathcal{G} \langle exp[i \int_{t_1}^{t_1+\tau} dt'\delta\omega(t')] \rangle_{ensemble} \tag{2.29}$$

In addition to the Ytterbrium atoms in the sample cell, there are also perturber atoms which can collide with the Ytterbrium atoms in their excited state. The many perturber atom interactions causing phase changes, $\delta\omega(t) = \sum_k \delta\omega^{(k)}$, can be written into this equation as

$$\langle \rho_{aa}^{(2)} \rangle_{time} = \mathcal{G} \langle \prod_{k=1}^{N_p} exp[i \int_{t_1}^{t_1+\tau} dt'\delta\omega^{(k)}(t')] \rangle_{ensemble} \tag{2.30}$$

to take into account the energy changes due to collisions with the $k-th$ perturber atom. At the operating pressures in the sample cell, the perturber atoms density, η_p, $\eta_p b_0^3 \ll 1$. This implies that there are no overlaps in collisions with the

$\delta\omega^{(k)}(t')$'s; interactions with the perturber atoms are independent and we have only binary collisions with the perturber atoms before the Ytterbium atom decays from the superposition state. This leads us to write equation 2.30 as

$$\langle\rho_{aa}^{(2)}\rangle_{time} = \mathcal{G}[\langle exp[i\int_{t_1}^{t_1+\tau} dt'\delta\omega^{(k)}(t')]\rangle_{ensemble}]^{N_p} \tag{2.31}$$

If we assume the ensemble average on the right hand side of equation 2.31 is independent of k and t_1 as shown in the previous paragraph, we can rewrite this equation as

$$\langle\rho_{aa}^{(2)}\rangle_{time} = \mathcal{G}[\frac{1}{T}\int_{-\frac{T}{2}}^{\frac{T}{2}} dt_1 exp(i\int_{t_1}^{t_1+\tau} dt'\delta\omega^{(1)}(t'))]^{N_p} \tag{2.32}$$

which leads to

$$\langle\rho_{aa}^{(2)}\rangle_{time} = \mathcal{G}[1-\frac{1}{T}\int_{-\frac{T}{2}}^{\frac{T}{2}} dt_1\{1-exp[i\int_{t_1}^{t_1+\tau} dt'\delta\omega^{(1)}(t')]\}]^{N_p} \tag{2.33}$$

and finally, rewritten in terms of many collisions during time, T,

$$\langle\rho_{aa}^{(2)}\rangle_{time} = \mathcal{G}[1-\frac{1}{T}\sum_{c}\int_{sc} dt_1\{1-exp[i\int_{t_1}^{t_1+\tau} dt'\delta\omega^{(1)}(t')]\}]^{N_p} \tag{2.34}$$

where the integral, $\int_{sc}$, is the integral over dt_1 for a single collision. The summation can be converted into an integral since

$$\#collisions \approx T\frac{v_r}{V}2\pi b db \tag{2.35}$$

This gives us the opportunity to substitute for the $\frac{1}{T}\sum_{sc}$ term in equation 2.34 as follows

$$\langle\rho_{aa}^{(2)}\rangle_{time} = \mathcal{G}[1-\frac{v_r}{V}\int_{0}^{\infty} 2\pi b db\int_{sc} dt_1\{1-exp[i\int_{t_1}^{t_1+\tau} dt'\delta\omega^{(1)}(t')]\}]^{N_p} \tag{2.36}$$

If we define the term $g(\tau)$ as

$$g(\tau) = v_r \int_0^\infty 2\pi b db \int_{sc} dt_1 \{1 - exp[i \int_{t_1}^{t_1+\tau} dt' \delta\omega^{(1)}(t')]\} \tag{2.37}$$

Equation 2.36 can be reduced to

$$\langle \rho_{aa}^{(2)} \rangle_{time} = \mathcal{G}[1 - \frac{1}{V} g(\tau)]^{N_p} \tag{2.38}$$

Since $\frac{1}{V} \ll 1$, this equation further reduces to

$$\langle \rho_{aa}^{(2)} \rangle_{time} = \mathcal{G}[e^{-\frac{g(\tau)}{V}}]^{\eta_p V} \tag{2.39}$$

which finally reduces to

$$\langle \rho_{aa}^{(2)} \rangle_{time} = \mathcal{G} e^{\eta_p g(\tau)} \tag{2.40}$$

If we substitute the expression $\mathcal{G}$ back into the equation, this leaves us with

$$\langle \rho_{aa}^{(2)} \rangle_T = (\frac{-\rho_D^{(0)}}{4})(\frac{-\gamma_a^{-1}}{T}) \int_{-\infty}^{\infty} d\tau e^{-\frac{\gamma_a|\tau|}{2}} e^{i\Delta\tau} I(\tau) e^{-\eta_p g(\tau)} \tag{2.41}$$

where

$$I(\tau) = \int_{-\infty}^{\infty} dt' \chi^*(t' + \tau) \chi(t') \tag{2.42}$$

where $g(\tau)$ is averaged over the relative velocity of the radiating atom and perturber atom and

If we evaluate the $g(\tau)$ in the impact collision limit where $\tau \gg \tau_{coll}$, equation 2.37 becomes

$$g(\tau) \to g_{IM}(\tau) = v_r \int_0^\infty 2\pi b db [1 - exp(i[\int_{-\infty}^{\infty} dt \delta\omega^{(1)}(t - t_{coll}, b, v_r)\tau]) \tag{2.43}$$

where the final integral term gives us the information on the net phase change of the collisions. We can solve this equation directly, yielding

$$g_{IM} = \frac{(\gamma \mid \tau \mid -i\delta\tau)}{\eta_p} \tag{2.44}$$

If we evaluate the $g(\tau)$ in the quasi-static limit where $\tau \ll \tau_{coll}$, equation 2.37 becomes

$$g_{QS}(\tau) = v_r \int_0^\infty 2\pi b db \int_{-\infty}^\infty dt[1 - exp(i\delta\omega^{(1)}(t - t_{coll}, b, v_r)\tau)] \tag{2.45}$$

where the final integral term gives us the information on how the phase changes during the collision; or in other words, how the coherence is affected by the collision.

2.3 Fluorescence Signal

The fluorescence signal per unit volume is proportional to the ρ_{aa} or the density of atoms in the excited state. In the phase-interrupting collision experiment described in chapter 1, we are working with two pulses in the sample cell. The first pulse excites the Ytterbrium atom to the ${}^3P_1$ state, which then evolves in time. We are looking for the interference of the macroscopic polarization of the Ytterbrium sample caused by the second pulse arriving in the sample cell after a time, τ_{delay}, after the first pulse as the signal output. The fluorescence rate equation can be written as

$$W_{fluor}(\tau_{delay}) = [\gamma_a \eta \langle \rho_{aa}^{(2)} \rangle T]_{Doppler} \tag{2.46}$$

where W_{fluor} is the function of the delay time between the successive pulses. We also write the Δ adjusted for the Doppler shift as

$$\Delta = \Omega - \omega_0 + \vec{k} \cdot \vec{v} \tag{2.47}$$

iWe are looking for the fluorescence signal of the interference of two laser pulses, so $\chi(t)$ of equation 2.6 can be re-written as a function of two pulses in terms of the normalized envelop $\mathcal{E}(t)$ as

$$\chi(t) = (\frac{\mu_{ab}E_0}{\hbar})[\mathcal{E}(t) + \mathcal{E}(t - \tau_{delay})e^{i\Omega\tau_{delay}}] \tag{2.48}$$

Substituting in for the various quantities from sections 2.1 and 2.2 into equation 2.46, the fluorescence rate equation becomes

$$W_{fluor}(\tau_{delay}) = [(\frac{\tau_{pulse}}{T})\eta(\frac{\mu_{ab}E_0}{\hbar})^2 \int_{-\infty}^{\infty} d\tau e^{\frac{-\gamma_a|\tau|}{2}} e^{i\Delta\tau} i(\tau) e^{-\eta_p g(\tau)}]_{Doppler} \tag{2.49}$$

where $i(\tau)$ is

$$i(\tau) = \frac{1}{\tau_p \chi_0^2} \int_{-\infty}^{\infty} dt' \chi(t') \chi^*(t' + t) \tag{2.50}$$

or alternatively

$$i(\tau) = \frac{1}{2\tau_{pulse}\chi_0^2} I(\tau) \tag{2.51}$$

and $\chi_0 \equiv \frac{\mu_{ab}E_0}{\hbar}$ as we did above in section 2.1. We can introduce the term $F(\tau_{delay})$ as

$$F(\tau_{delay}) \equiv \frac{1}{\tau_{pulse}} [\int_{-\infty}^{\infty} d\tau e^{i\Delta\tau} e^{-\frac{\gamma_a|\tau|}{2}} i(\tau) e^{-\eta_p g(\tau)}]_{Doppler} \tag{2.52}$$

then the fluorescence rate equation becomes

$$W_{fluor}(\tau_{delay}) = [(\frac{\tau_{pulse}}{T}\eta(\frac{\mu_{ab}E_0}{\hbar})^2 \tau_{pulse} F(\tau_{delay})]_{Doppler} \tag{2.53}$$

where $I(\tau)$ now becomes a function of the two pulse from equation 2.48

$$I(\tau) = \mid \frac{\mu_{ab}E_0'}{\hbar} \mid^2 \int_{-\infty}^{\infty} dt' [\epsilon(t') + \epsilon(t' - \tau_{delay})e^{i\Omega\tau_{delay}}][\epsilon(t' + \tau) + \epsilon(t' + \tau - \tau_{delay})e^{i\Omega\tau_{delay}}] \tag{2.54}$$

due to the presence of the two pulses as in the case of $\chi(t)$ in equation 2.48 above. If we try $\epsilon(t) = e^{-\frac{(\frac{t}{\tau_p})^2}{2}}(\pi)^{-\frac{1}{4}}$, $I(\tau)$ becomes (after some algebra)

$$I(\tau) = \left| \frac{\mu_{ab} E_0'}{\hbar} \right|^2 \tau_p [2e^{-(\frac{\tau}{2\tau_p})^2} + e^{i\Omega\tau_{delay}} e^{-(\frac{\tau_{delay}+\tau}{2\tau_p})^2} + e^{-i\Omega\tau_{delay}} e^{-(\frac{\tau_{delay}-\tau}{2\tau_p})^2}] \qquad (2.55)$$

In order to study the phase-interrupting collisions in the quasi-static limit we must have $\tau_{pulse} \ll \tau_{coll}$. Likewise, to continue the study in the impact collision limit, we must further have the $\tau_{delay} \gg \tau_{coll}$.

If we assume that $ku \ll \frac{1}{\tau_{pulse}}$, we find that equation 2.52 becomes

$$F(\tau_{delay}) = \frac{1}{\tau_{pulse}} \int_{-\infty}^{\infty} d\tau I_s(\tau) e^{-\eta_p g_{QS} \tau} + \cos(\omega - \delta)\tau_{delay} e^{(\frac{ku}{2})^2 \tau_{delay}^2} e^{-\gamma\tau_{delay}} \qquad (2.56)$$

for $\tau_{delay} \gg \tau_{coll}$. In the experiment, we find that for $u = \sqrt{\frac{2k_B T}{m}}$, $ku \sim 1$ Ghz and for τ_{pulse} on the order of a picosecond, $\frac{1}{\tau_{pulse}} \sim 10^3$ Ghz; then the assumption, $ku \ll \frac{1}{\tau_{pulse}}$, is a valid one.

If we define the term C as

$$C = \frac{1}{\tau_{pulse}} \int_{-\infty}^{\infty} d\tau I_s(\tau) e^{\eta_p g_{QS}(\tau)} \qquad (2.57)$$

where g_{QS} is defined in Section 2.2, equation 2.56 can be written as

$$F(\tau_{delay}) = C + \cos(\omega - \delta)\tau_{delay}[e^{-(\frac{ku}{2})^2 \tau_{delay}^2}][e^{-\gamma\tau_{delay}}] \qquad (2.58)$$

The $g_{QS}(\tau)$ gives us the information on the processes that go on during the collision, which is the intended purpose of the phase-interrupting collision experiment. This requires that we have a laser pulsewidth much less than the duration of the collisions, τ_{coll}, time between successive pulses, τ_{delay} and all of these times must be much less than t_{spon} of the Ytterbrium atom to allow study of the processes before the Ytterbrium atoms radiatively return to their normal state.

2.4 Laser System Requirements

These equations in section 2.3 give us the total fluorescence that the Ytterbium atoms can yield during collisional processes. The signal that can be detected by experimental apparatus remains significantly lower. For example, only a portion of the Ytterbium atoms will absorb the incident laser pulses and be excited to the superposition state. Likewise, we will only detect that portion of the radiated fluorescence that strikes the face of the detection apparatus. The signal that could be detected by the photomultiplier tube of the experiment in these limits is given by

$$P_{fluor} = (P_{in})(\alpha L)(\frac{\tau_{pulse}}{\tau_{spon}})RF(\tau_{delay}) \tag{2.59}$$

where P_{in} is the input power of the laser at the sample cell, αL is the absorption coefficient of the Ytterbium sample of the laser pulse as it transverses the sample cell of length L, R is the geometry factor dealing with the PMT detection device only receiving a portion of the total fluorescence signal transmitted through the proper solid angle to strike the detector face, and $F(\tau_{delay})$ is the actual interference pattern formed from the autocorrelation of the laser pulses with the radiator-perturber interaction. The $F(\tau_{delay})$ was derived in the previous section and is given by

$$F(\tau_{delay}) = C + [\cos(\omega - \delta)\tau_{delay}][e^{-(\frac{hu}{2})^2\tau^2_{delay}}][e^{-\gamma\tau_{delay}}] \tag{2.60}$$

Inside $F(\tau_{delay})$, the C is given by equation 2.61 and is that portion of the fluorescence signal due to quasi-static limit.

$$C = \frac{1}{\tau_{pulse}}\int_{-\infty}^{\infty} d\tau I_s(\tau)e^{-\eta_p g_{QS}(\tau)} \tag{2.61}$$

and g_{QS} is given by

$$g_{QS} = \langle v_r \int_0^{\infty} 2\pi b db \int_{-\infty}^{\infty} dt[1 - e^{i\delta\omega^{(1)}(t-t_{coll},b,v_r)\tau}]\rangle_{v_r} \tag{2.62}$$

The cosine and exponential terms inside the the brackets of $F(\tau_{delay})$ represent the contributions to the fluorescence signal by the impact collision limit. Equation 2.59

demonstrates the outline of the requirements for the laser system. As we decrease the pulsewidth, τ_{pulse} , to achieve the $\tau_{coll} \gg \tau_{pulse}$ required to approach the quasi-static and impact collision limits to gain information on the dynamic aspects of the collisions, we must increase the input power, P_{in} in direct proportion to maintain the same relative fluorescence signal. As τ_{pulse} becomes much smaller than the other time scales, the accuracy of the approximations becomes greater and more details of the collisions can be discerned. From the previous data taken with a picosecond regime laser that was shown in figure 1-2 on 12, we see the need to further decrease the pulsewidth to get more detailed information on the collision processes.

Likewise, given the initial power at the sample cell on the order of a few microwatts, we also see the need to increase the laser power while maintaining the shortened pulse width and shape. As the signal to noise ratio is high for this experiment, we must further increase the size of the signal to discern details from the background noise. This requires a laser system that can produce a sub-picosecond pulse with a resulting output power at the sample cell at least several times greater than the previous seven microwatts.

Chapter 3

Sub-Picosecond Lasers

This chapter covers the theory of sub-picosecond laser systems of the hybrid synchronously pumped dye laser type. The discussion of saturable absorbers and pulse compression along with hybrid laser theory sets the theoretical framework of the experiment. Again, the extended mathematical derivations for formulas will not be explicitly shown in every detail; the pertinent details will be shown along with the supporting references for further information. The mathematical formulation of the theory for the hybrid synchronous pumped dye laser was developed from a series of published articles by Z.A. Yasa [Yasa1983], J.M. Catherall [Catherall et al1982] and J. Herrmann [Herrmann1982].

3.1 Saturable Absorber

The use of the saturable absorber medium is a common occurence in dye laser applications and its theory is relatively straight forward and developed extensively in published material. The processes are similar to the mechanisms involved in standard dye laser operation. The basic model was developed by L.M. Frantz in the early 1960's [Frantz1963] and further refined for the ultra-short pulse regime by G.H.C. New [New1972][New1974] for the two level saturable absorber system and by N.J. Frigo [Frigo1983] for the four level saturable system. The development of the saturable absorber theory will not be delved into as part of this thesis, but will be discussed in general terms to gain a basic understanding of the resulting effects. The reader is invited to peruse these listed articles for further discussion and mathematical development of the saturable absorber theory if desired.

Saturable absorbers work as a mechanism to clean up the pulse shape by absorbing unwanted portions of the pulse as the it transverses the laser cavity. When set at the proper saturable absorber concentration and dye jet location, the saturable absorber absorbs the leading edge of the pulse envelope up to the point where the saturable absorber medium becomes saturated. The dye medium then becomes transparent to the pulse and passes the remaining pulse energy in the pulse envelope through the dye jet to propagate. The remaining energy in the envelope redistridutes itself within the remaining pulse envelope and causes the peak amplitude to rise as the pulse transits the dye jet. This effect creates an increase of several times the original input pulse amplitude and causes an effective decrease of the Full Width Half Maximum (FWHM) point, thereby decreasing the pulse width. The shaping of the pulse continues as the dye pulse continues to pass through the laser cavity until the pulse is finally transmitted through the output coupler out of the laser cavity. In some cases where cavity length is not perfectly matched to the laser wavelength or there are imperfections in the laser's mirrors, a dye pulse may form that does not approach the theoretical secant-shaped pulse. These pulses may be skewed or have ancillary "wings" of satellite pulses as shown in figure 3-1 on page 35. The formation of satellite pulses is discussed later in this chapter in section 3.2.3. The saturable absorber works to externally shape the dye laser pulse within the laser cavity to approach the theoretical hyperbolic $secant^2$ pulse shape.

The saturable absorber is selected based on its absorption cross-section at the laser output wavelength and the dephasing or relaxation time, T_2 of the absorber. We want to maximize the absorption cross-section so that we can use the lowest concentration of saturable dye. This is important because although saturable absorbers effectively shape the pulse, they also reduce the output power of the laser by as much as 75 percent, depending on the saturable absorber absorption cross-section and dye concentration. If we assume a two level saturable absorber molecule, the saturation

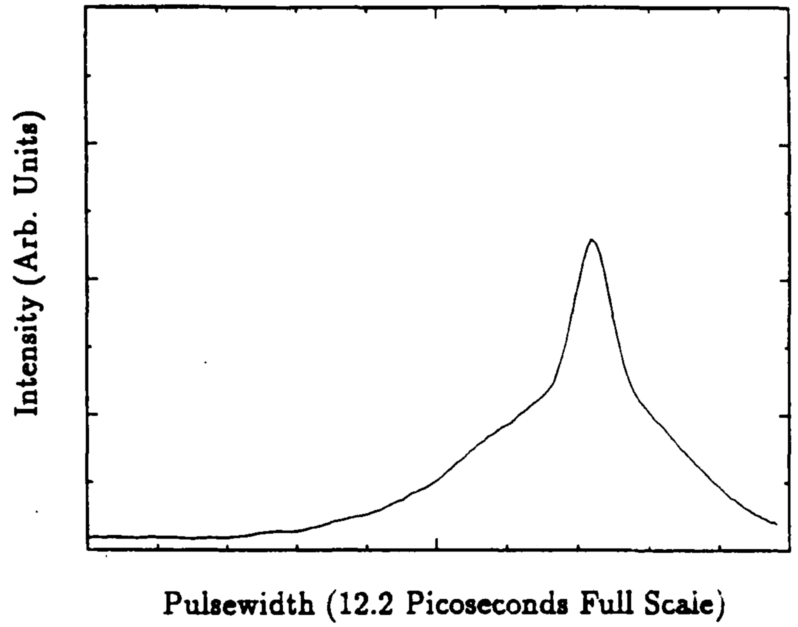

Figure 3-1: Initial Dye Pulse with Ancillary Wings

intensity or I_{sat} for the saturable absorber is given by

$$I_{sat} = \frac{\hbar\omega}{2\sigma_h^u(0)T_2} \tag{3.1}$$

where σ_h^u is the absorption cross-section of the saturable absorber at the dye laser wavelength. The I_{sat} must be set at a some fractional point of the peak pulse amplitude to maximize effective pulse shaping and the transmitted pulse power. We also want a saturable absorber with a relatively fast relaxation time or γ_{sp} as to enable a fast recovery time for the next pulse. If the saturable absorber does not relax quickly enough in the saturable absorber dye stream, it remains transparent to the next laser dye pulse and the laser dye pulse passes through unmodified by the saturable absorber. We can obtain the the spontaneous lifetimes and absorption cross-sections from the absorption charts from the manufacturers of the dyes for specific wavelengths and saturable absorber dye concentrations. The starting point for the saturable absorber concentrations in the dye stream was set at the point where

$$n\sigma_{abs}l \sim 1 \tag{3.2}$$

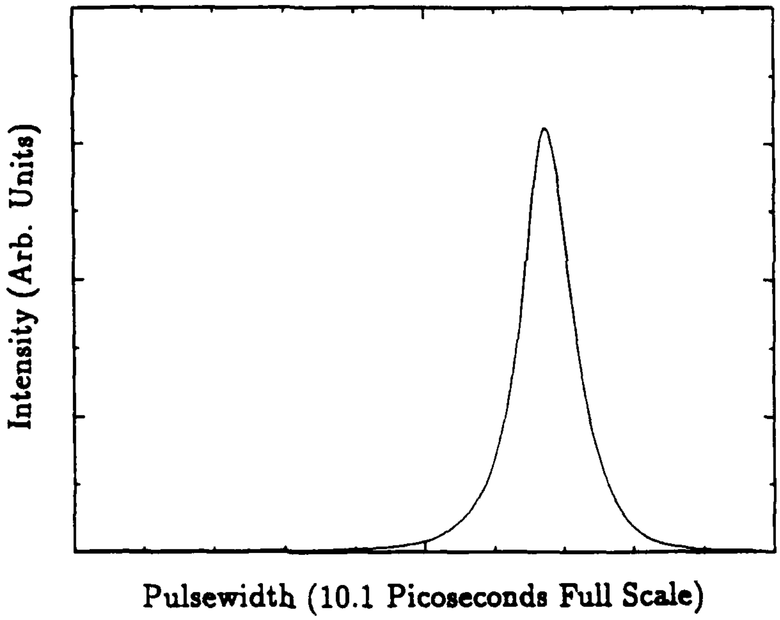

Figure 3-2: Saturable Absorber Modification of Pulse Shape and Width

where l is the thickness of the dye stream for the saturable absorber. We used this starting point to vary the saturable absorber concentrations about in order to more effectively control the pulse shape and width to achieve optimum results.

In figure 3-2, the original pulse of figure 3-1 has been modified through the absorption of a portion of the laser dye pulse by the saturable absorber dye jet. This resulting pulse has a higher amplitude and narrower pulsewidth and the final pulse shape approaches the theoretical hyperbolic *secant*^{2} shape.

In many traditional laser systems, the saturable absorber is combined with the lasing dye in the lasing dye jet. The hybrid synchronously pumped dye laser uses separate dye and saturable absorber jets to achieve optimum mode-locking and pulse shaping characteristics. This technique enables external modification of the fully developed dye pulse within the laser cavity and eliminated any secondary pulses that are formed after the passage of the initial dye pulse through the laser cavity.

3.2 Hybrid Synchronously Pumped Lasers

ADVANTAGES	DISADVANTAGES
Relatively easy to use	Requires separate dye and saturable absorber jets
Wavelength tunable over wide range	Sensitive to saturable absorber concentration and location
Produces pulsewidth in the half picosecond regime	No group velocity dispersion compensation
Can be cavity dumped	
Can be developed with existing laser components	

Table 3.1: Hybrid Synchronously Pumped Dye Laser

There are a variety of mode-locking techniques available to achieve picosecond regime pulses within a laser cavity. The hybrid synchronously pumped laser consists of separate laser dye and saturable absorber jets within the dye laser cavity. This laser system offers the shortest pulse length (near sub-picosecond regime) available without resorting to the multi-prism system in the ring cavity. The advantages and disadvantages of this system are shown in table 3.1 on page 37. Although this system does require a greater number of components and changes in saturable absorber dye concentrations for differing wavelengths, it does offer the potential to achieve the characteristics that are outlined in section 2.4 for the laser system requirements. It does not offer the shortest pulses, but can be tuned to our required wavelength. Although ring cavity or CPM passive mode-locked laser has produced the shortest pulse on record [Couillaud1985], it suffers from low power output and little or no frequency tunability; thus making the ring cavity system unsuitable for the phase-interrupting collision experiment.

For these reasons, the hybrid synchronously pumped laser was selected for use in the experiment.

3.2.1 Laser Gain Equation

The standard gain equations for typical dye laser operation fully apply to the hybrid synchronously pumped laser with several modifications. We can write the standard gain equation for dye laser operation as [Yasal1975]

$$\frac{dG}{d\tau} + \sigma G[I(\tau)(G-1) - I_p(\tau)] = 0 \tag{3.3}$$

where G is the gain, τ is the local time for the development of the dye pulse, $I(\tau)$ is the intensity of the dye pulse and I_p is the intensity of the pump laser pulse. Likewise, we can write the dye pulse intensity as simply

$$I(\tau) = I_p G(\tau) \tag{3.4}$$

The modifications to this gain and intensity equations come from the physical arrangement of the laser components in the hybrid synchronous pumped dye laser cavity. First, the separate saturable absorber jet induces additional cavity losses within the laser cavity as part of the $(1-R)$ regime. The separation of the dye and absorber jets allows for full development of the pulse shape within the dye jet and laser cavity without any interference from the saturable absorber.

Second, the saturable absorber jet externally induces pulse amplitude, shape and width changes to the pulse as it transverses the dye cavity prior to emission. This external pulse-shaping allows for better control of the pulsewidth and shape.

The standard dye laser uses a three mirror folded dye cavity and is pumped by an external pump laser. In the experimental setup, the pump laser emits a continuous output of mode locked pulses at a 76 Mhz repetition rate. A dye laser pulse is created when the cavity lengths of the pump laser and dye laser are set almost equal to each other. In general for the hybrid synchronously pumped laser, this cavity mismatch, Δ, must be less than $10\mu m$, in order for the laser to achieve optimum mode-locking and pulse shaping [Couillaud1985]. Experimental evidence shows that pulses on the order of one picosecond can be achieved with a cavity mismatch of less than $2\mu m$ and the stability of the pulsewidth depends directly on maintaining the cavity mismatch [Ryan et al1978]. As the cavity mismatch becomes much less than the pulsewidth, a stable dye laser pulse occurs with a pulse width less than the incoming pump laser pulsewidth. This implies that by shortening the pulsewidth of the pump laser pulse, we can also decrease the pulsewidth of the resulting dye laser pulse. The stability of the pump laser pulse plays a key role in maintaining the stability of the dye pulsewidth and pulse shape [Yasa1983].

For a sufficiently short laser pump pulse and long enough dye laser cavities, we can neglect the fluorescence of the pump pulse interfering with the dye pulse as the excited dye molecules will decay to the ground state prior to the return of the dye pulse to the dye jet from the output mirror. We must assume that the hybrid laser is aligned such that the pump and dye pulses are co-linear through the dye jet. The full development of the gain and intensity equations taking the above characteristics into consideration is covered in Appendix A. The resulting laser dye pulse intensity equation takes the form of

$$I(\tau) = R_l G(\tau) I(\tau - \Delta) + I_{sp}[G(\tau) - 1] \tag{3.5}$$

where R_l represents the linear cavity loss including the saturable absorber. The spontaneous emission effects essentially shift the dye pulse forward to offset the increased retardation due to the cavity mismatch, Δ. As Δ increases, the stability of the conserved pulse shape dramatically decreases and the resulting pulsewidth dramitically increases.

3.2.2 Steady State Pulse Characteristics

In an ideal hybrid synchronously pumped dye laser, the spontaneously emitted dye pulse caused by a pump pulse of intensity I_p, builds up in an ultra-fast time period and achieves a steady state which satisfies equation 3.5. The development of the steady state dye pulse takes place over three separate regions shown in figure 3-3 on

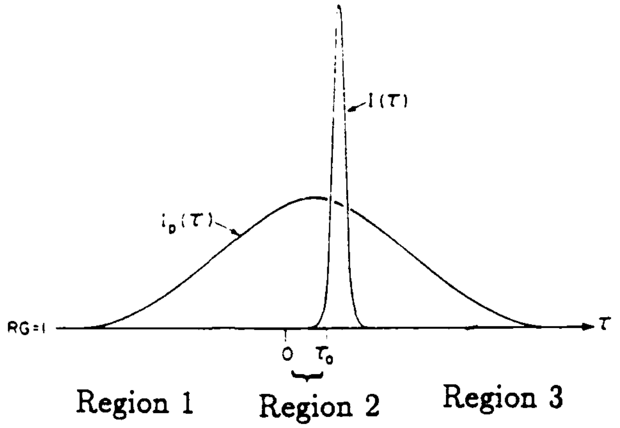

Figure 3-3: Development of the Steady State Dye Pulse

page 40.

In these regions defined for a local time, τ, where in Region 1, $\tau \leq 0$, Region 2 $\tau = \tau_0$ or the threshold time where $R_lG(\tau = 0) = 1$ and the dye pulse is created and Region 3 where $\tau \geq 0$, different mechanisms contribute to the development of the dye pulse. The horizontal line, $R_lG(\tau) = 1$, represents the threshold gain condition for the formation of the dye pulse as a function of the pump pulse. In region 1 where $\tau \leq 0$, spontaneous emission effects dominate in the development of the pulse. The dye pulse intensity reaches a steady state intensity given by

$$I(\tau \leq 0) = I_{sp}\{G(\tau)(1-R_l)[1+R_lG(\tau 1-\Delta)[1+R_lG(\tau-2\Delta)[1+R_lG(\tau-n\Delta]]]-1\} \quad (3.6)$$

and likewise in Region 2 where $\tau = 0$, the dye pulse intensity reaches a steady state intensity given by

$$I(\tau = 0) = I_{sp}\{G(\tau)(1-R_l)[1+R_lG(-\Delta)[1+R_lG(-2\Delta)[1+R_lG(-n\Delta]]]-1\} \quad (3.7)$$

Equations 3.6 and 3.7 converge to a value of $I(0)$ where $I(0) \gg I_{sp}$. Finally, in Region 3 where $\tau \geq 0$, we find the dye pulse intensity is much greater than the pump pulse intensity and reaches a steady state pulse intensity given by

$$I(\tau \geq 0) = R_l G(\tau) I(\tau - \Delta) \tag{3.8}$$

where $G(\tau)$ is a solution to

$$\frac{dG}{d\tau} + \sigma G[I(\tau)(G-1) - I_p(\tau)] = 0 \tag{3.9}$$

In the previous section, it was shown that the dye pulse monotonically increases with τ until it becomes much larger than the pump pulse within a very short time after τ_0. In general, the pump pulse tends to increase the gain in the laser cavity while the dye pulse tends to saturate or deplete the gain. We find that in Region 3, the $I(t)$ of the dye pulse quickly depletes the increased gain of the laser dye jet caused by the the pump pulse $I_p(t)$ and the dye pulse then dominates in the laser cavity.

Equations 3.8 and 3.9 demonstrate the characteristics that the conserved pulseshape must have. To solve for the shape of the pulse, one must use the initial conditions for a given Δ , $G(0) = \frac{1}{R_l}$ and $I(0)$ from equation 3.5 and solve them simultaneously using an iterative technique [Catherall et al1982].

We know that the total gain, G, is a function of the round trip gains, G_1 and G_2, and that the return trip gain depends on the total pulse energy from the previous sections. The threshold time $\tau = 0$ is determined from the total pulse energy. In order to determine the relationship between τ_0, the start time for the dye pulse and Δ, we must solve the $I(\tau)$ equation above for $n\Delta$ steps between $\tau = 0$ and $\tau = \tau_0$ giving

$$I(n\Delta) = R_l^n G(n\Delta \ldots G(\Delta) I(0) \tag{3.10}$$

If we use $G(\tau) = G_1(\tau)G_2(\tau_0)$, $G_1(\tau) = G_o X_p(\tau)$ and neglect ground state absorption ($G_o = 1$ from section 3.2.1), this equation finally yields

$$I(n\Delta) = I(0)[R_l G_2(\tau_0)]^n e^{\sigma \sum_{k=1}^{n} E_p(k\Delta)} \tag{3.11}$$

Using $n\Delta = \tau$, this becomes

$$I(\tau) \simeq I(0)[R_l G_2(\tau_0)]^{\frac{\tau}{\Delta}} e^{\frac{\sigma}{\Delta} \int_0^{\tau} E_p(\tau) dt} \tag{3.12}$$

If we assume that the pump pulse remains relatively constant over the Δ intervals, this equation yields

$$I(\tau_0) = I(0)[(R_l G_2(\tau_0))^{\tau_0} e^{\sigma \int_0^{\tau_0} E_p(t) dt}]^{\frac{1}{\Delta}} \tag{3.13}$$

We can develop an approximate numerical solution to this equation by substituting variables $t = \tau - \tau_0$, $I(\tau_0) = I_0$ and $G(\tau_0) = G_0$. From the previous sections, we can ignore the I_p of the pump pulse in the steady state Region 3. We know that the steady state pulse must satisfy

$$I(t + \Delta) = R_l G(t) I(t) \tag{3.14}$$

If we re-define $G(t)$ as $G(t) = e^{g(t)}$, use the substituted variables and the same methods above, equation 3.13 becomes

$$I(t) = I_0[R_l^t e^{\int_0^t g(t')dt'}]^{\frac{1}{\Delta}} \tag{3.15}$$

for slowly varying gains over periods of Δ. For small pulse energies, the gain of the dye jet is only slightly reduced by the dye pulse and the gain equation 3.9 can be approximated as

$$\frac{dG}{dt} + \sigma G I(t)(G_0 - 1) = 0 \tag{3.16}$$

which yields the solution

$$g(t) = g_0 - \sigma \int_0^t (G_0 - 1) I(t') dt' \tag{3.17}$$

Combining this solution with equation 3.15 yields

$$I(t) = I_0 e^{2\int_0^t [\frac{ln(R_l G_0)}{2\Delta} - \frac{(G_0-1)}{2\Delta}\int_0^{t'} \sigma I(t'')dt''] dt'} \tag{3.18}$$

If we define $E(t) = \int_0^t I(t')dt'$, we now have

$$\frac{dE}{dt} = I_0 e^{2\int_0^t (\frac{ln(R_l G_0)}{2\Delta} - \frac{(G_0-1)}{2\Delta}\sigma E) dt'} \tag{3.19}$$

If we differentiate this equation with respect to t again and rearrange terms we get

$$\frac{dE}{dt} - I_0 = 2\frac{ln(R_l G_0)}{2\Delta}E - \frac{(G_0-1)}{2\Delta}E^2 \tag{3.20}$$

which is in the form of the Ricatti equation. If we define the term $\mathcal{A} = [(\frac{ln(R_l G_0)}{2\Delta})^2 + \frac{(G_0-1)}{2\Delta}\sigma I_0]^{\frac{1}{2}}$, the solution to this equation yields

$$E(t) = I_0 \frac{1 - e^{-2\mathcal{A}t}}{\mathcal{A} - \frac{ln(R_l G_0)}{2\Delta} + (\mathcal{A} + \frac{ln(R_l G_0)}{2\Delta})e^{-2\mathcal{A}t}} \tag{3.21}$$

If we differentiate again and rearrange terms, we get the solution to the pulse shape as

$$I(t) = \frac{\mathcal{A}^2}{\sigma\frac{(G_0-1)}{2\Delta}} Sech^2(\mathcal{A}[t - \frac{ln(\frac{\mathcal{A}+\frac{ln(R_l G_0)}{2\Delta}}{\mathcal{A}-\frac{ln(R_l G_0)}{2\Delta}})}{2\mathcal{A}}]) \tag{3.22}$$

If we define

$$I_m = \frac{\mathcal{A}^2}{\sigma\frac{(G_0-1)}{2\Delta}} \simeq \frac{(lnR_l G_0)^2}{2\sigma\Delta(G_0-1)} \tag{3.23}$$

and

$$t_m = \frac{ln(\frac{\mathcal{A}+\frac{ln(R_l G_0)}{2\Delta}}{\mathcal{A}-\frac{ln(R_l G_0)}{2\Delta}})}{2\mathcal{A}} \tag{3.24}$$

the solution to the pulse shape becomes

$$I(t) = I_m Sech^2[\mathcal{A}(t - t_m)] \tag{3.25}$$

The FWHM pulsewidth is then

$$t_p = \frac{1.7627}{\mathcal{A}} \simeq \frac{3.5\Delta}{ln(R_l G_0)} \tag{3.26}$$

with the peak of the pulse occurring at $t = \tau_0 + t_m$.

In the steady state, both pulse shape and pulse energy are conserved. This is shown for pulse energy as

$$\int_{-\infty}^{\infty} I_f(\tau)d\tau = \int_{-\infty}^{\infty} I(\tau)d\tau = E(\tau = \infty) \tag{3.27}$$

Remembering that in the steady state after n round trips, the spontaneous emission effects can be neglected and $G(\tau)$ in equation A.18 and $I_f(\tau + \Delta)$ in equation A.21 can be substituted into the above equation yielding

$$X^{\frac{1}{R_l}} = 1 + G(\tau_0)(X - 1) \tag{3.28}$$

for the conserved pulse energy. Substituting in for $G(\tau_0)$, we get

$$X^{\frac{1}{R_l}} = 1 + G_o G_1(\tau_0)(X - 1)\left(\frac{X X_p}{[1 + G_1(\tau_0)(X - 1)]}\right)^{\gamma} \tag{3.29}$$

We know that $\sigma E(\tau = \infty) \ll 1$, and equation 3.29 yields the first order solution for the conserved pulse energy.

$$\sigma E(\tau = \infty) = \frac{2R_l(R_l G_o G_1(\tau_0) X_p^{\gamma} - 1}{1 + R_l^2 G_o G_1(\tau_0) X_p^{\gamma}(1 - 2\gamma[G_1(\tau_0 - 1])} \tag{3.30}$$

3.2.3 Satellite Pulses

Another characteristic of hybrid synchronously pumped laser is that their cavity mechanisms create the potential for the formation of a secondary satellite pulse from the initial pump pulse. A high energy pump pulse can create a satellite pulse after the main pulse if it has sufficient energy remaining after passing the laser dye medium to reach a threshold level for the secondary pulse formation. The threshold condition exists when at the end of the dye laser pulse, the gain of the laser dye medium is depleted to a level defined as the saturation gain, G_{sat}, equal to

$$G_{sat} = \frac{G(\tau_0)X(\tau)}{1 + G(\tau_0)(X(\tau) - 1)} \tag{3.31}$$

where

$$X(\tau) = e^{\sigma E(\tau)} \tag{3.32}$$

After the main pulse is created, the $G(\tau)$ continues to increase due to the "excess" remaining energy in the pump pulse. This gain increase follows the form

$$\frac{dG}{d\tau} + \sigma G[I(\tau)(G-1) - I_p(\tau)] = 0 \tag{3.33}$$

For $\tau \geq \tau_0$ for the high energy pump pulse, the gain, $G(\tau)$ becomes

$$G(\tau) = G_{sat} e^{\sigma[E_p(\tau) - E_p(\tau_0)]} \tag{3.34}$$

The satellite pulse is created when the $R_l G(\tau = \infty) > 1$ at $\tau = \tau_s$. This condition can also be written in terms of equation 3.34

$$R_l G_{sat} e^{\sigma[E_p(\infty) - E_p(\tau_0)]} > 1 \tag{3.35}$$

The positioning and generation of the satellite pulse at τ_s is based on the system's given Δ, and the solutions to τ_0, $G(\tau_0)$ and X from the steady state gain conditions in section 3.2.2 above. The satellite pulse can be eliminated by increasing the linear cavity losses, R_l, to effectively shift the relative positioning of τ_0 and τ_s to the end of the pump pulse [Yasa1983]. In the hybrid synchronously pumped dye laser, this increased cavity loss is accomplished through the use of the separate saturable absorber dye jet at a position further along the dye pulse path within the laser cavity. Careful positioning of the dye jet along with the appropriate saturable absorber dye concentration can eliminate or minimize the formation of the satellite pulse.

3.3 Pulse Compression

An external pulse compression apparatus can be used to further shorten the laser pulse output from teh hybrid synchronously pumped laser. The basic procedure is a simple two step process. First, the output pulse must be spectrally broadened or "chirped" through a nonlinear refractive medium such as a Kerr medium. Traditionally, fiber optics have been used as the Kerr medium for most pulse compression apparatus. The second step of the process involves compressing the pulse using a dispersive delay line consisting of a pair of diffraction gratings.

3.3.1 Chirping the Pulse

The input pulse amplitude envelope from the hybrid synchronously pumped laser transmitted to the Kerr medium of the pulse compression apparatus is assumed to be a complex variable, V, and of the form

$$V(z=0,t) = A\sec(t/t_0) \tag{3.36}$$

where the time variable, t, is a retarded time defined such that for a given distance along the Kerr medium, z, the center of the pulse is at $t=0$. The peak amplitude A, is defined by

$$A = \sqrt{P/P_1} \tag{3.37}$$

and where P is the peak power of the input pulse and P_1 is the peak power of the fundamental soliton for the Kerr medium [Tomlinson1984]. P_1 is defined by

$$P_1 = \frac{nc\lambda A_{eff}}{16\pi z_0 n_2} \times 10^{-7} W \tag{3.38}$$

where n is the refractive index for the core of the Kerr medium, n_2 is the nonlinear coefficient for the Kerr medium in electrostatic units, and A_{eff} is the effective area of the core of the fiber optic that the chirped pulse transverses. z_0 is a normalized optical fiber length defined by

$$z_0 = 0.322\frac{\pi^2 c^2 \tau_0^2}{\mid D(\lambda) \mid \lambda} \tag{3.39}$$

where τ_0 is the intensity full width half maximum (FWHM) of the input pulse and is approximaely equal to $1.76t_0$. $\mid D(\lambda) \mid$ is the dimensionless group velocity dispersion (GVD) of the input pulse. The GVD acts to linearize the chirping of the pulse over the length of the Kerr medium such that virtually all input power appears in the compressed pulse. There is a trade-off between optimum pulse compression and optimum pulse shape, and fiber length must be closely monitored to optimize both characteristics of the compressed pulse [Grischkowsky1983] . z_{opt} is the actual optical fiber length required to spectrally double the input pulse for optimal pulse compression. This length effectively saturates the fiber, and fiber lengths beyond this optimal z_{opt} serve to degrade the optimal pulse compression and shape. The actual GVD of the input pulse for the synchronously pumped laser need not be explicitly calculated as experimental evidence shows that these equations can be numerically approximated by the following equations [Kaiser1988]

$$\frac{\tau_0}{\tau} \approx 0.63A \tag{3.40}$$

$$\frac{z_{opt}}{z_0} \approx \frac{1.6}{A} \tag{3.41}$$

3.3.2 Compressing the Pulse

The second part of the pulse compression procedure involves the compression of the chirped pulse using diffraction gratings. The actual compresser is simply a delay line with a frequency dependent delay [Tomlinson1984]. Using the Fourier transform of the initial input pulse amplitude envelope, $V(z,t)$, we find

$$V(z,\omega) = A(\omega)e^{i\Phi(\omega)} \tag{3.42}$$

where $A(\omega)$ and $\Phi(\omega)$ are real functions (neglecting explicit z dependence). The compressed pulse in frequency domain is given by

$$V_c(z,\omega) = A(\omega)exp\{i[\Phi(\omega) + \Phi_c(\omega)]\} \tag{3.43}$$

where $\Phi_c(\omega)$ is a phase function of the compressor and is of the form

$$\Phi_c(\omega) = \Phi_0 - a\omega^2 \tag{3.44}$$

a is the grating compressor constant and is given by

$$a = \frac{b\lambda^3}{4\pi c^2 d^2 \cos^2(\gamma)} \tag{3.45}$$

where b is the distance between diffraction gratings, d is the groove spacing, λ is the center wavelength of the pulse and λ is the angle of incidence of the pulse on the grating. Again, this can be numerically approximated by [Kaiser1988]

$$a \approx 0.52\tau_0^2 A \tag{3.46}$$

For a perfect compressor at $t = 0$, $\Phi_c(\omega) = -\Phi(\omega)$, all frequency components of the pulse are in phase, and the optimum shortened pulse is achieved with the maximum peak amplitude. In actual practice, these approximations are in general agreement with experimental results.

3.3.3 Numerical Estimate

We can use the equations developed in the sections above to find the theoretical limits for the external pulse compression apparatus. The initial trials with the laser system with the cavity dumper produced an average output power of 4 milliwatts with a pulsewidth of 5 picoseconds while operating at the 556 nanometer wavelength. If we use these figures as a base figure for the calculations, these parameters give a z_{opt} of 1.27 meters for the fiber optic, a diffraction grating separation, b, of 1 meter and the resulting theoretical output pulsewidth of 260 femtoseconds.

Chapter 4

Equipment

This chapter describes the laser dyes, saturable absorbers, laser systems and equipment used during the experiment. A preliminary discussion of background work on the system is included to demonstrate the parameters of the experiment.

4.1 Chemical Dyes

The selection of the various organic chemical dyes for lasing and saturable absorber dyes was dictated by the requirements for the phase-interrupting collision experiment and the equipment available for use in the laboratory. Final selection and experimentation was based on the thorough research of available publications.

4.1.1 Laser Dye

The availability of the second harmonic Nd:YAG laser for the experiment dictated the selection of Rhodamine 590, $C_{28}H_{31}N_2O_3Cl$, for the phase-interrupting collision experiment. Rhodamine 6G, the regularly used field nomenclature, is a commonly used laser dye when dissolved in etheylene gylcol for use in pulsed and CW laser operation. The absorption curve for the Rhodamine 6G dye is shown in figure 4-1 on page 51. The peak fluorescence for Rhodamine 6G dissolved in ethylene glycol is at 580 nanometers when pumped with the second harmonic Nd:YAG laser. This dye's lasing curve goes from 552 to 592 nanometers as an operating range. This

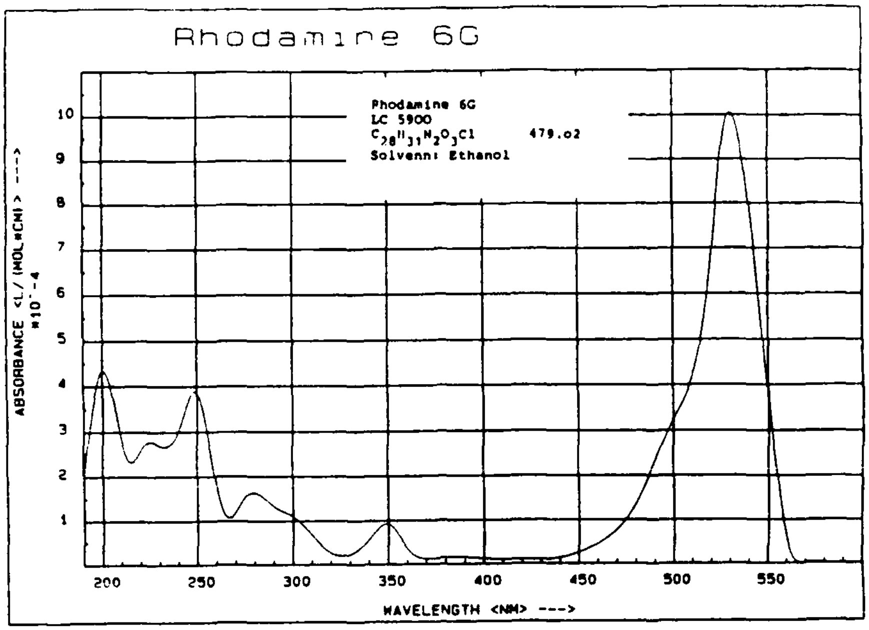

Figure 4-1: Rhodamine 6G Absorption Curve [Lambda1986]

combination produces a dye laser conversion efficiency of 33 percent at the peak, then drops off dramatically off of the curve [Lambda1986]. Note that the 555.6 nanometer wavelength for the experiment is operating at the extreme edge of the dye gain curve. Therefore, a relatively high pump laser powers is required in order to obtain the desired high output power at the required 555.6 nanometer wavelength. Rhodamine 110 was another candidate for the lasing dye as it has a peak fluorescence at 560 nanometers when pumped with the third harmonic output of the Nd:YAG pump laser. Since this pump laser option was not available to us, we were obligated to use the Rhodamine 6G dye with the Nd:YAG second harmonic pumping and accept the lower efficiency.

4.1.2 Saturable Absorbers

A wider variety of chemical dyes for use as saturable absorbers was available at the 555.6 nanometer wavelength. The three primary candidates were DODCI, DTCI and DMETCI. All dyes used ethylene glycol as a solvent and initially had several milliliters of methanol added to aid in dissolution. The methanol quickly evaporated

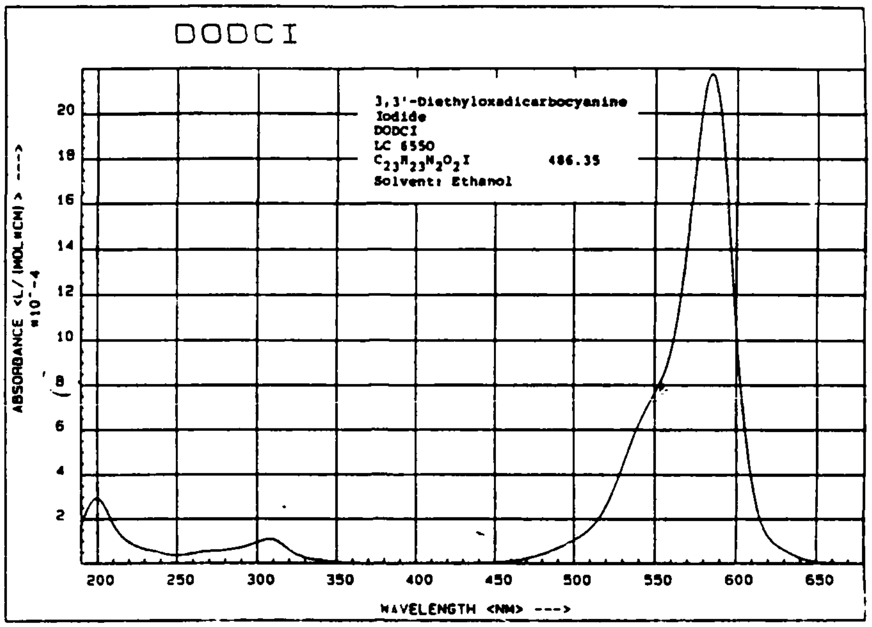

Figure 4-2: DODCI Absorption Curve [Lambda 1986]

during normal operation which resulted in the solvent being almost pure ethylene glycol. Each candidate dye was evaluated for its performance in based on its characteristics at the desired wavelength in accordance with the guidelines discussed in Chapter 3. The absorbance depicted in the following figures can be used to determine the homogeneous absorption cross-section σ_h^u, used in the saturable absorber theory section by the following equation.

$$\sigma_h^u = \frac{10^7 a}{Avagado's\#} \tag{4.1}$$

where a is the absorbance value from the figure. Final selections for the saturable absorber were made on the basis of which saturable absorber characteristics were optimal for the desired wavelength.

DODCI, $C_{23}H_{23}N_2O_2I$ was selected as a trial candidate for the laser saturable absorber because it is a traditional saturable absorber for Rhodamine 6G. Its absorption curve characteristics has a peak absorption cross section at 582 nanometers when dissolved in ethanol [Lambda1986]. The dye's absorbance at 556 nanometers is $8.1\frac{L}{Mol\bullet CM} \times 10^{-4}$ which yields a $\sigma_h^u = 1.34 \times 10^{-16}$ cm^2 which places this third

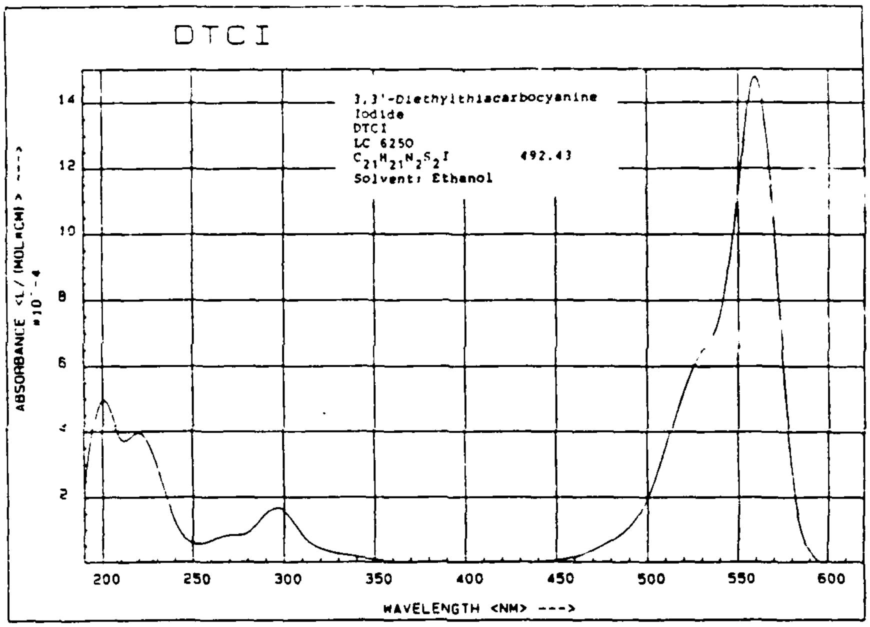

Figure 4-3: DTCI Absorption Curve [Lambda1986]

among the three candidates for this wavelength. DODCI's dephasing time, T_2, is on the order of 300 picoseconds [Watanabe et al1983][Rulliere1976].

It has the best absorption characteristics at 580 nanometers with an absorption cross section of 3.73×10^{-16} cm^2. It is frequently used with Rhodamine 6G dye as a saturable absorber because of the compatability of the DODCI's absorption curve with Rhodamine 6G's lasing frequencies. The absorption curve for the DODCI chemical dye is shown in figure 4-2 on page 52.

DTCI, $C_{21}H_{21}N_2S_2I$ was another possible candidate due to its peak absorption cross section at 557 nanometers when dissolved in ethanol [Lambda1986]. The optimum performance for this dye is in the 560 nanometer region for flash lamp pumped Rhodamine 6G lasers used in pulsed operations. The absorption cross section for the DTCI dye at 556 nanometers is 2.13×10^{-16} cm^2. The high absorption cross section initially made this the leading candidate for effective pulse shaping. However, initial trials with this saturable absorber early in the experiment and further research showed that the DTCI has a long relaxation time (on the order of 760 picoseconds [Maeda1972]) that adversely affects its performance in the ultra-fast pulse regime .

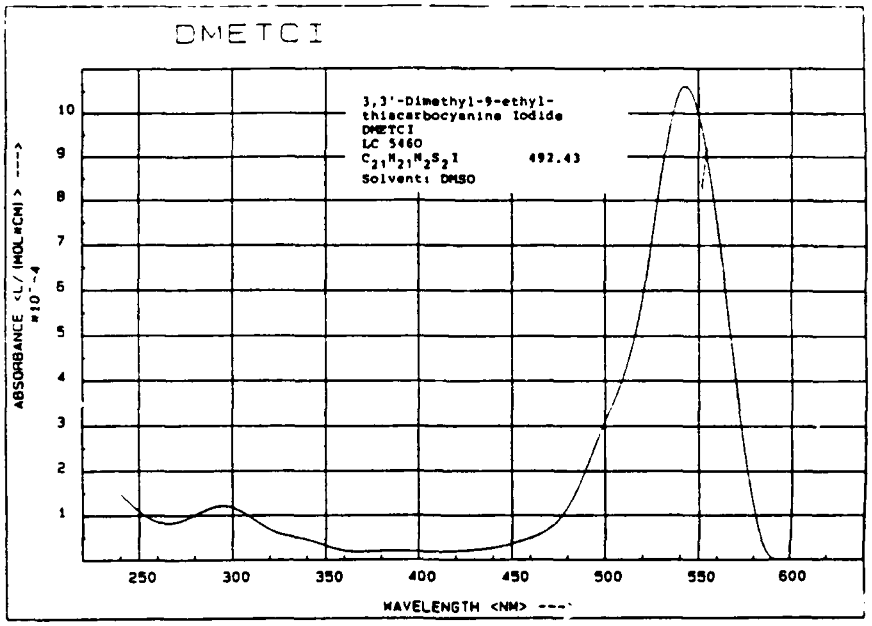

Figure 4-4: DMETCI Absorption Curve [Lambda1986]

The absorption curve for the DTCI dye is shown in figure 4-3 on page 53.

DMETCI, $C_{21}H_{21}N_2S_2I$ has its peak absorption at 540 nanometers when dissolved in DMSO [Lambda1986]. The absorption cross section for 556 nanometers is 1.54×10^{-16} cm^2 which is the second highest cross-section. This dye is operating at the edge of its spectrum curve when used at 556 nanometers, yet the high absorption cross section at this wavelength still makes it a viable candidate for optimum pulse shaping. DMETCI's dephasing time, T_2 is not well known but is estimated to be on the order of 250 picseconds [Sibbett1982].

The 580 nanometer wavelength is out of range of the absorption curve for this dye. The absorption curve for the DMETCI dye is shown in figure 4-4 on page 54.

Based on these characteristics, DODCI was selected for testing the hybrid synchronously pumped dye laser for its optimum performance at 580 nanometers and DMETCI was selected for the saturable absorber for the laser system to operate at the required 556 nanometer wavelength.

4.2 Laser System

The primary laser to be used in the phase-interrupting collision experiment was a Nd:YAG pumped chemical dye pulsed laser. Initially, the Coherent Antares 76-S Nd:YAG laser, using the factory Mode Locker and Second Harmonic Generator, produced an output of 2.1 Watts at the wavelength of 532 nanometers. This laser operated at a repetion rate of 76 Mhz and produced a pulse with a pulsewidth of 5 picoseconds. The output of the pump laser was coupled to a hybrid synchronously pumped dye laser consisting of two conventional dye laser set in series along on Invar rod. The first dye laser was used as the lasing mechanism while the second dye laser was used as the saturable absorber mechanism. The lasing mechanism was a Coherent Model 590 Dye laser using the Rhodamine 6G dye dissolved in ethylene glycol. Concentration of the Rhodamine 6G dye in solution was set at 4.0 x 10_{-4} Molar based on previous records for optimal power output at the 555.6 nanometer wavelength. A second Coherent Model 590 Chemical Dye laser without the pump mirror was used in the chemical dye laser cavity as a synchronously pumped saturable absorber. The saturable absorber Model 590 was further modified to allow translation of the saturable absorber jet along the beam path. This faciliated the optimal placement of the saturable absorber jet for maximum effectiveness. Initially, a Coherent Model 7220 Cavity Dumper was used as an output device with the laser system. The repetition rate for the Cavity Dumper was varied between 1 MHz and 38 Mhz to optimize power output of the laser system and signal peak at the sample cell. Resulting output power varied between 4 mW at 1Mhz and 38 Mw at 38 Mhz. Initial trials with the collision experiment showed that the power output with the Nd:YAG-Laser Dye-Saturable Absorber-Cavity Dumper system was not yielding sufficient power at the sample cell to discriminate the details of the phase-interrupting collisions from the background noise. The Coherent High Power Second Harmonic Generator using a KTP crystal as the doubling mechanism was then installed on the Coherent Model 76-S and peak power for the pump laser was then increased to 3.2 watts which yielded approximately 54 mW at the 555.6 nanometer wavelength. This

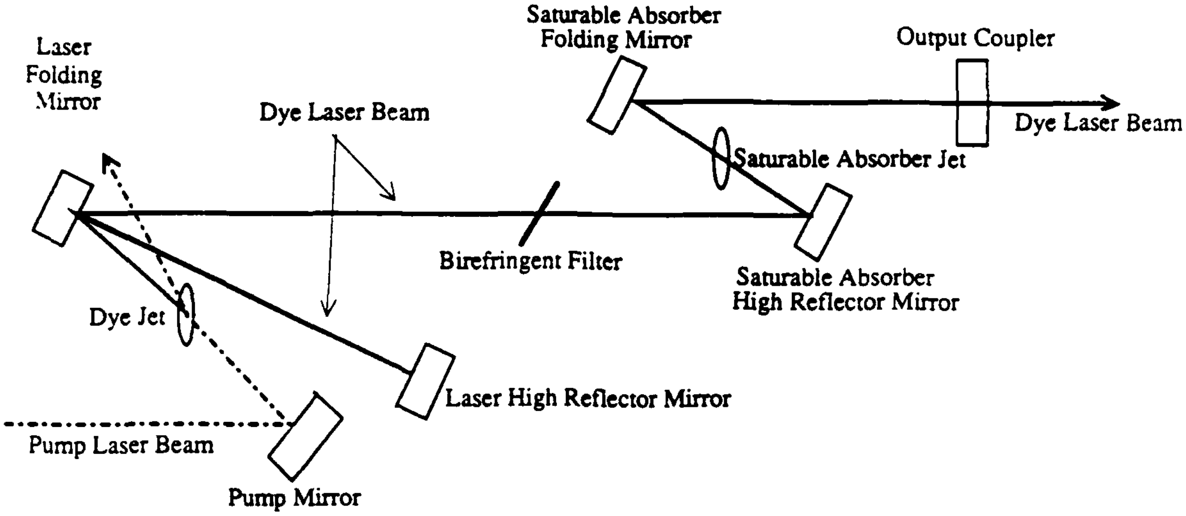

(Figure not to scale)

Figure 4-5: Hybrid Synchronously Pumped Dye Laser Diagram

physical setup and resulting power level still did not produce a sufficent fluorescent signal at the sample cell to discern the details of the phase-interrupting collisions from the background noise. Another complication was discovered in that the power from the Antares 76-S pump laser was not stable and would randomly fluctuate on the order of three to five percent in the infrared power, creating a fluctuation of six to ten percent at the 532 nanometer wavelength and a similar resulting fluctuation in the dye laser output. This fluctuation created difficulties in generating the repeatability of the experiment.

The next step on the process was to remove the Coherent Cavity Dumper and replace this ouput device with an output coupler with a reflectivity, R, equal to 97 percent at the 556 nanometer wavelength. In addition, the Coherent High Power Second Harmonic Generator was replaced with a JTT Crystal Company heated LbO crystal as the second harmonic generator. LbO offers the advantage that it has a higher damage threshold than KTP, although it does not double as efficiently. The LbO doubling crystal comes with its own temperature control mechanism to optimize the power output. The crystal was mounted on a fabricated mount which allowed translation of the crystal assembly along the beam path to place the crystal in the focus of the internal telescope assembly of the laser to produce differing output power levels. Additionally, this JTT LbO crystal offers the advantage of being temperature-dependent for optimal second harmonic generation rather than angle-dependent as in the case of the standard KTP crystal. The LbO crystal operates most efficiently within a narrow temperature range which must be adjusted occasionally to optimize performance as the crystal absorbs infrared light from the laser and achieves differing thermal equilibriums. This final arrangement of the laser system is depicted in figure 4.2 on page 56 and was used for the experiment. The pump power fluctuation from the Antares 76-S laser was reduced to less than three percent and the output power of the pump laser was easily maintained at 3.2 watts. The pump laser could be adjusted for a power output of up to 4 watts for possible future needs if this increased level of power is required. The final output of the basic Nd:YAG-Laser Dye-Output Coupler system (before experimentation with the use of various saturable absorber dyes and concentrations) was a two picosecond pulse with an average power output on the order of 140 milliwatts.

4.3 Pulse Compression

The physical layout of the pulse compression device is shown in figure 4-6 on page 58. The fiber optic used as the chirping medium is the Newport Model F-SPA-10 Single Mode Polarization Preserving Fiber. This fiber has a central core with a diameter of 4 microns and a jacket diameter of 250 microns. This fiber's transmission characteristics were optimal for the pulse compression at the 556 nanometer wavelength.

4.3.1 Apparatus

The chirping mechanism of the pulse compression apparatus consisted of a Newport Model F-916 Multi-Axis Fiber Positioner with a 20X objective lens that was used to hold the F-SPA-10 fiber optic and focus the incoming laser pulse on the fiber core. A

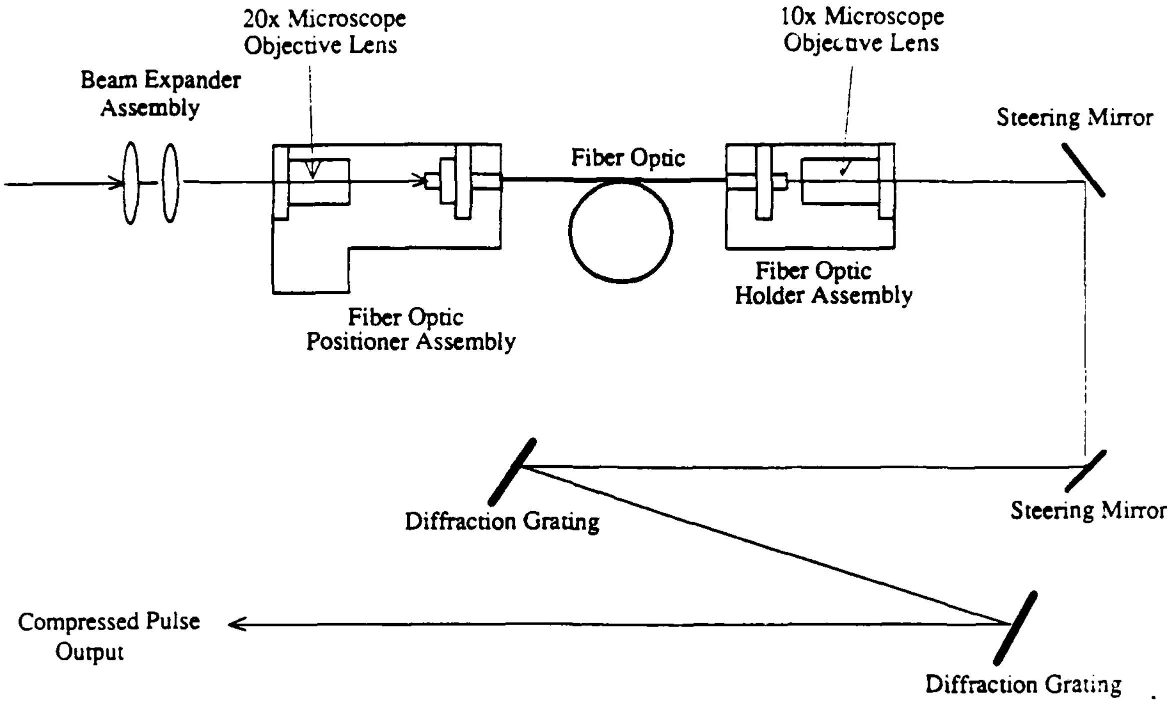

Figure 4-6: Pulse Compression Setup

2.5X beam expander was used to optimize the beam waist to focus on the fiber core. A mechanical holder using polyethylene piping was used to support the fiber length, the calculated z_{opt}, to minimize stress induced losses from the core. The output device was a NRC Model FP-1 Fiber Holder coupled with 10X objective lens to expand the beam waist for the compressor.

The compressor mechanism of the pulse compression apparatus consisted of a pair of diffraction gratings separated by the calculated distance b . The gratings were the PTR Optics High Resolution First Order Grating with a groove spacing of 600 lines per millimeter. This gives the d equal to 1.67×10^{-4} centimeters for the grating pair constant equation 3.45 on page 48.

4.3.2 Initial Pulse Compression Results

The initial calculations in section 3.3.2 gave a resulting theoretical output pulsewidth of 260 femtoseconds for the external pulse compression apparatus. Experimental results gave reasonable agreement with the theory. The trials with the pulse compression apparatus gave an approximately 300 femtosecond pulsewidth using Rhodamine

6G dye with the DMETCI saturable absorber in the hybrid synchronously pumped dye laser. Coupling losses of 30 percent of the output of the dye laser to the fiber optic combined with the 40 percent loss at each diffraction grating drastically reduced the available power to go through the experimental setup for the phase-interrupting collision experiment to the previous levels where the details of the collisions could not be discerned. The coupling losses were attributed to improper focusing of the incident light on the fiber core and preparation of the fiber ends; the faces of the fiber had to be cleaved perfectly flat in order to achieve a theoretical 80 percent coupling. Losses due to the diffraction gratings are a nature of the diffraction mechanism and cannot be reduced. The pulse compression aspect of the experiment was temporarily put to the side to concentrate on optimizing laser power output and pulse shape and width characteristics solely through the hybrid synchronously pumped laser cavity. Theoretical work in Chapter 3 demonstrsted that the pulse shape and width can be sufficiently controlled through the laser cavity to allow initial observation of collisional data. If initial results with the hybrid dye laser system require further refinement of the pulsewidth, this can be accomplished through the further decreasing of the pulsewidth through this external pulse compression apparatus.

4.4 Electronics

A variety of equipment was used during the course of the experiment. A significant portion of it was fabricated by Kyungwon An and other previous graduate students to suit the specific needs of the phase-interrupting collision experiment and was available to be used in this thesis project.

4.4.1 Determination of Laser Wavelength

The laser wavelengths that the hybrid synchronously pumped dye laser produced were determined by passing the output laser beam through a Jarrell Ash Model 82-410 Interferometer. This device was calibrated using the 514.5 and 488 nanometer wavelengths produced by a Coherent Model 52B Argon Ion CW Laser, the 486 nanometer wavelength produced by a Spectra Physics Model 155 He-Ne CW laser, and the 532 nanometer wavelength produced by the Antares Model 76-S Nd:YAG pulsed Laser.

4.4.2 Recording Pulse Shapes

The mechanism for recording the pulse shapes was a fabricated auto-correlator using a solenoid driven by a sine-wave generator. This setup is shown in figure 5-1 on page 63. The output of the auto-correlator was directed into a second harmonic generator crystal to a photo-multiplier tube. The two beam output of the autocorrelator was adjusted such that a pulse shape was formed only as a product of the two incident beams. A pinhole was used a spatial filter to ensure that other laser light did not produce a second harmonic signal which could strike the PMT detector face.

This output was processed through a fabricated integrating amplifier and collected into the computer.

Data collection was done by the use of the Asyst Version 2.0 program run on an Standard Model 286 computer. Kyungwon An wrote the "Sampling.002" program to sweep the PMT to record the data into the 256 data bin storage channels.

4.4.3 Real Time Observation of Pulse Shapes and Widths

The data collection equipment described in section 4.4.2 above allowed the written collection of the data taken in the experiment. This recording procedure took several moments to set up and record the data on the computer terminal VDT screen for each iteration. Each variation of the experimental parameters required a myriad of adjustments to be made to the mirrors and saturable absorber jet of the hybrid synchronously pumped dye laser to optimize pulse shape, pulse width and output power for each variation. A auto-correlator using a solenoid was used to allow real-time observation of the pulse shape and width. The laser system output was put though a beamsplitter which directed $\frac{1}{2}$ the laser beam into the auto-correlator setup and the remainder of the beam into the data collection equipment as shown in figure 5-1 on page 63. The laser beam was monitored using a photo-multplier tube assembly connected to a Textronics Type RM 503 oscilloscope for the auto-correlator output display. Calibration of the oscilloscope screen was done through the monitoring of the solenoid's travel range, then converting that range into a time scale for the screen. Variations in the solenoid travel was done through Heath Schlumberger Model SG-18A Sine-Square Audio Generator powered by a Kepco Model KS6-10M Regulated DC Power Supply.

This real-time observation system enabled the optimization of the laser system's controls to optimize the pulse characteristics rapidly without stopping to record the information until the best possible pulse characteristics were achieved, then record the data without disturbing the experimental setup or laser controls.

Chapter 5

Data Acquisition

This chapter details the experimental setup and preliminary actions taken prior to the actual conduct of the experimental trials as well as the mechanisms and procedures used during the data taking process.

5.1 Setup

The experimental physical setup is shown in figure 5-1 on page 63. The equipment used in this experimental setup is described in detail in section 4.2 for the laser system, section 4.3 for the pulse compression apparatus and section 4.4 for the electronic system in chapter 4 .

5.2 Preliminary to Data Acquisition

The majority of the work involved in the prelimary experiments involved the optimization of the power output and maximizing the stability of the pump laser. The Coherent 76-S Nd:YAG pump laser requires about an hour of warm-up time to achieve internal thermal stability. After this period, the laser shutter can be opened and adjustments can be made to the cavity controls to optimize the power. The next step consists of optimizing the temperature controls of the JTT LbO doubling crystal to optimize power. This crystal requires about 20 minutes to achieve thermal stability

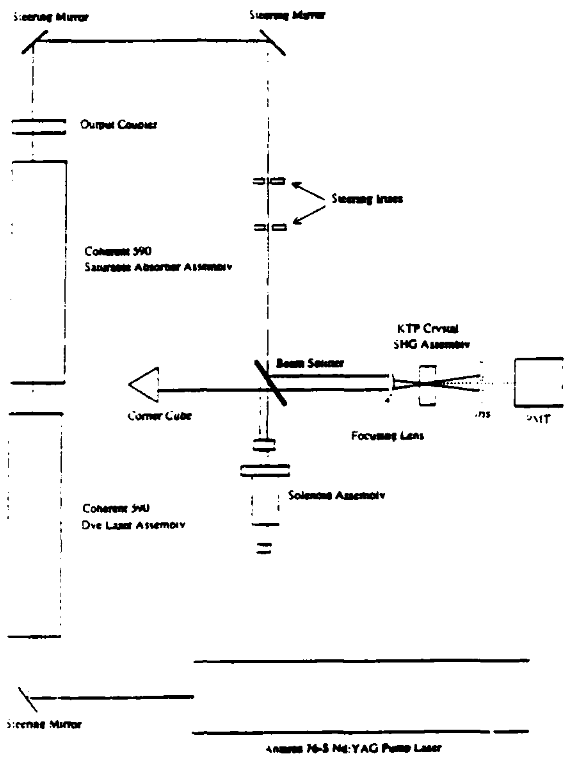

Figure 5-1: Experimental Setup

after the Antares 76-S shutter is open. The temperature control can be adjusted to improve power output, but another 20 minutes must be allowed after each adjustment to achieve a new thermal equilibrium before cavity adjustments can be made to optimize power again.

The next step involves ensuring that the dye laser and saturable absorber jets are working properly at the proper pumping pressure and that the lasing beam strikes the jets in the proper position for optimum performance. The power output of the hybrid laser is then monitored as the laser controls are adjusted to optimize power output and laser spot shape.

The final step involves turning on the various electronics and ensuring that the output laser beam strikes the autocorrelator and the PMT properly to allow simultaneous observation of the real time pulse and data collection. The solenoid travel length must be measured and monitored to ensure proper calibration of the experimental data and final results.

5.3 Data Acquisition

The procedures for data acquisition were relatively straight forward and the same sequence of procedures were followed for each trial to ensure uniform results. The wavelength of the laser output was checked to determine the wavelength of the laser output by using the interferometer and then tuned to the proper wavelength by using the birefringent filter on the dye laser.

The cavity length for the hybrid laser was adjusted to optimize pulse shape and width as seen on the oscilloscope. The pump power output from the Nd:YAG laser was then noted; the output power of the hybrid laser was recorded, then a data sample consisting of four pulses was recorded for each cavity detuning to allow for statistical variation, and finally the output power was again checked at the end of the sampling trial to ensure that the power had not changed more than five percent over the duration of the data acquisition period. The hybrid laser was then detuned again to try and optimize performance and the process was repeated. The pulsewidths shown for the figures throughout this thesis represent the average of the four pulseshapes taken for each sample for the best performance of the laser cavity tuning while the actual pulse shape shown represents the optimum shape of the trials.

For each data trial run, the laser system was tuned for optimum power as a synchronous pumped laser at the given pump power. The dye jet was then turned on and the laser system was then tuned for optimum performance as a hybrid synchronous pumped laser. The laser cavity length was then detuned for the optimal pulse shape as seen on the oscilloscope. The signal on the oscilloscope was then optimized by adjusting the steering mirrors into the autocorrelator and the autocorrelator components. The laser tuning adjustments were also adjusted to optimize shape and minimize the background noise. After the signal was optimized, the sample data was taken. After several different cavity detunings and data samplings were taken at the given trial iteration, the laser pump power was adjusted to a different level by using neutral density filters and the process was repeated for the new trial iteration. After the pump power was reduced to the level where the hybrid synchronous pumped laser would not efficiently lase, the saturable absorber concentration would be changed and was allowed to circulate in the saturable absorber jet system for at least 20 minutes before the laser alignment and tuning procedure would be started. This time period ensured that the new saturable absorber solution was thoroughly mixed and had reached an equilibrium concentration value equal to the desired value. The entire sequence would then be repeated for the full pump power range available until the hybrid synchronous pumped laser would no longer lase.

5.4 Data Analysis

The data taken during the experiment was analyzed using a series of programs, "Autoco.c" and "Analize.it", written by Kyungwon An. The data taken in the "Sampling" program does not exactly correspond to real-time observation. The "Sampling" program assumes that the solenoid travel of the autocorrelator travels at a uniform velocity and exactly in phase with the sine wave generator that drives the solenoid. In real time, there is a mechanical delay induced in the solenoid travel as it cycles through the complete range of motion and its velocity varies as a function of solenoid position. For example, when the solenoid is at the end of a cycle, its velocity is zero. The solenoid then accelerates through its full range of motion, then deccelerates as it reaches the end of its travel range until its velocity is zero again and the cycle is repeated. These two programs take this motion into consideration when processing the data taken in the experiment and produce the output shown in this thesis. These programs are included at Appendix B.

5.5 Experimental Procedure

The first phase of the experiment consisted of verifying and optimizing the performance of the hybrid synchronously pumped dye laser as an entity. To do this, we optimized the system characteristics using the dyes and equipment to operate in their peak performance ranges. For Rhodamine 6G, we operated at the 580 nanometer wavelength and used the traditional saturable absorber associated with Rhodamine 6G, DODCI. The second phase of the experiment consisted of optimizing the system characteristics at the required 555.6 nanometer output wavelength using Rhodamine 6G as the lasing dye and DMETCI as the saturable absorber.

Chapter 6

Experimental Results at 580 nanometer Wavelength

For the first phase, we used Rhodamine 6G as the lasing dye at its peak performance wavelength of 580 nanometers with the second harmonic Nd:YAG pumping. The standard Coherent Rhodamine 6G mirror optics were used in the Coherent 590 Dye laser to optimize laser performance with the exception of the saturable absorber high reflector mirror. We used a Rhodamine 110 high reflector mirror for this optical component as it was the closest available mirror. This mirror's optical coating cut off performance above 580 nanometers, so we were not able to operate at the very peak of Rhodamine 6G performance curve. The longest wavelength we were able to achieve with peak power was at 576 nanometers. The laser was first tuned to optimize performance and power as a standard dye laser without the saturable absorber in operation. The concentration of Rhodamine 6G dye in ethylene glycol was increased to 5.0×10^{-4} Molar so that 80 percent of the incident pump power was absorbed by the lasing dye jet. This absorption level is listed by the manufacturer as being the optimal point for dye laser operation and produced a peak average power of 780 milliwatts when tuned for maximum power output. The resulting pulse with the best possible pulse width and shape is shown in figure 6-1 on page 68. This pulse had a real pulsewidth of 2.21 picoseconds and a output power of 412 milliwatts at this cavity length detuning.

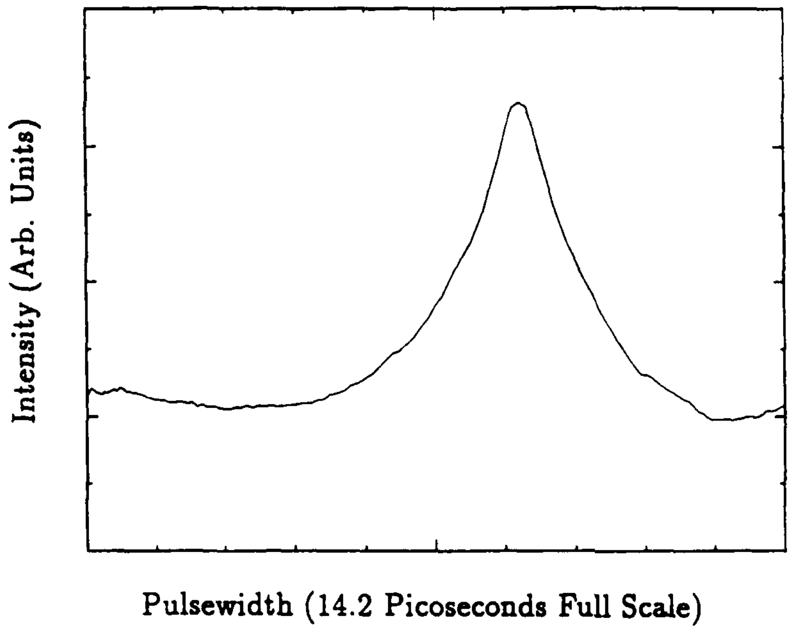

Figure 6-1: Rhodamine 6G Synchronous Pumped Dye Laser Output at 576 nanometers

The broad incoherent background around the coherence spike is due to the incoherent portion of the laser pulse. This can be reduced through the appropriate concentration of saturable absorber that absorbs this portion of the output laser pulse as discussed in the theory chapter. DODCI was selected as the saturable absorber to begin development of the hybrid synchronously pumped dye laser. It has a peak absorption cross-section of 3.65×10^{-16} cm^2 at the 576 nanometer wavelength. The initial concentration for the DODCI saturable absorber was set at the point where

$$n\sigma_{h}^{u} l \sim 1 \tag{6.1}$$

and the trials were varied in concentration about that point. The laser systems characteristics were then altered to optimize laser pulsewidth, shape and power output.

The best performance output at the 576 nanometer wavelength with 3 watts of pump laser produced a real pulsewidth of 1.87 picoseconds with a power of 94 milliwatts and is shown in figure 6-2 on page 69. The DODCI saturable absorber concentration was set at 2.25×10^{-4} Molar. Note the reduction in the incoherent portion of the pulse due to the DODCI saturable absorber jet.

We were not able to totally reduce the incoherent background noise of the laser

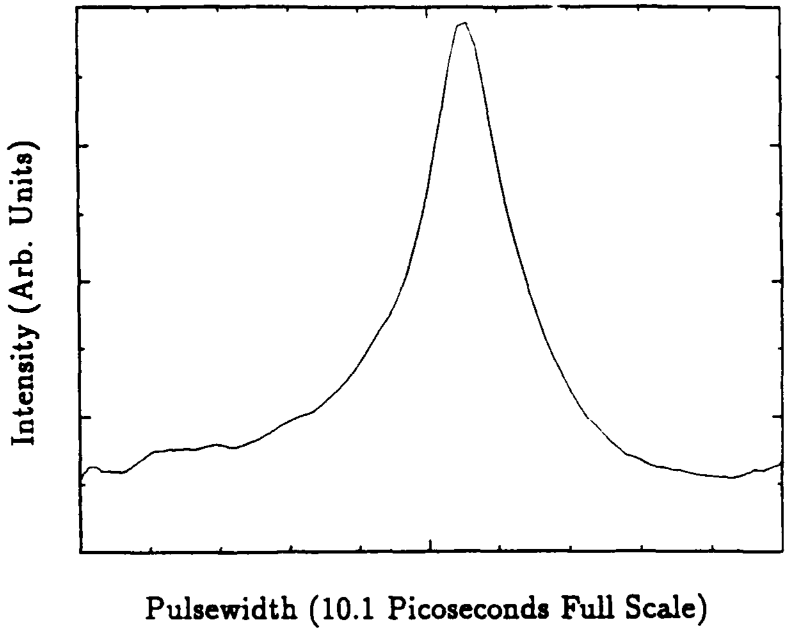

Figure 6-2: Optimum Performance for 3.0 watt pumped Hybrid Synchronously Pumped Dye Laser with DODCI Saturable Absorber at 576 nanometers

pulse which indicated that we were not fully passively modelocking the laser pulse in the laser cavity and producing the best possible output pulse. We then investigated several possibile explanations why the laser's potential to produce shortened pulsewidths with optimal shapes was limited. The first possibility that was investigated was that we were over-saturating the saturable absorber. With the output coupler having a transmission coefficient of 5%, we were able to calculate the intracavity intensity of the lasing cavity. Knowing the focus of the saturable absorber high reflector mirror (2.5 cm) and the laser beam waist on this mirror (.05 cm ±.01 cm), we were able to calculate the intensity of the laser at the saturable absorber jet. The power inside the cavity, P_{in}, is equal to

$$P_{in} = \frac{P_{out}}{T} \tag{6.2}$$

which yields a P_{in} equal to 1.88 watts. The P_{in} is related to the peak laser power inside the laser cavity by

$$P_{in}^{peak} \approx \frac{P_{in}}{\tau_{pulse}\frac{\#pulses}{s}} \tag{6.3}$$

For a laser repetion rate of 76 Mhz and τ_{pulse} before the saturable absorber effects equal to 2.21 picoseconds, this yields a P_{in}^{peak} equal to 1.11×10^4 W. To calculate the peak intensity, I_{in}^{peak}, we must find the laser spot size on the dye stream. By using

$$\omega = \frac{\lambda f}{\pi \omega_0} \tag{6.4}$$

we find that the laser spot size on the dye jet is 1.83×10^{-3} cm. The peak intensity inside the laser cavity is then

$$I_{in}^{peak} = \frac{P_{in}^{peak}}{\pi \omega_0^2} \tag{6.5}$$

which yields $1.06 \times 10^9 \ \frac{W}{cm^2}$ or in cgs units, $1.06 \times 10^{16} \ \frac{erg}{s-cm^2}$. The I_{sat} for DODCI can be found by using equation 3.1

$$I_{sat} = \frac{\hbar \omega}{2\sigma_u^h T_2} \tag{6.6}$$

for $\sigma_u^h = 3.65 \times 10^{-16} \ cm^2$ from the figure 4-2 and the T_2 equal to 300 picoseconds [Watanabe et al1983], this yields a I_{sat} equal to $2.51 \times 10^{12} \ \frac{erg}{s-cm^2}$ which is much less than the $I_{in}^{peak} = 1.05 \times 10^{16} \ \frac{erg}{s-cm^2}$ calculated above. This indicated that we were oversaturating the saturable absorber stream and not achieving optimum passive mode-locking of the laser pulse in the dye laser cavity. We evaluated the possibility was that the absorption curve for the DODCI saturable absorber shown on page 52 was shifted due to the ethylene glycol solvent. Figure 4-2 represents the absorbance of DODCI as a function of wavelength when dissolved in ethanol. Ethylene glycol is a better candidate for a saturable absorber jet because it has a higher viscosity and produces a more stable dye stream. This same higher viscosity also produces a red-shift of the absorption spectrum as the dye molecules suspended in solution are more rigidly fixed. A sample of DODCI was then dissolved in first ethanol and then ethylene glycol and analyzed through the use of ultra-violet / visible absorbance spectrometer to determine the resulting change in the absorption curve. The results are depicted in figures 6-3 for ethanol and figure 6-4 for ethylene gylcol.

These figures depicts the absorbance value ϵ as a function of wavelength. The absorbance curves clearly show that the peak of the absorbance curve has been shifted

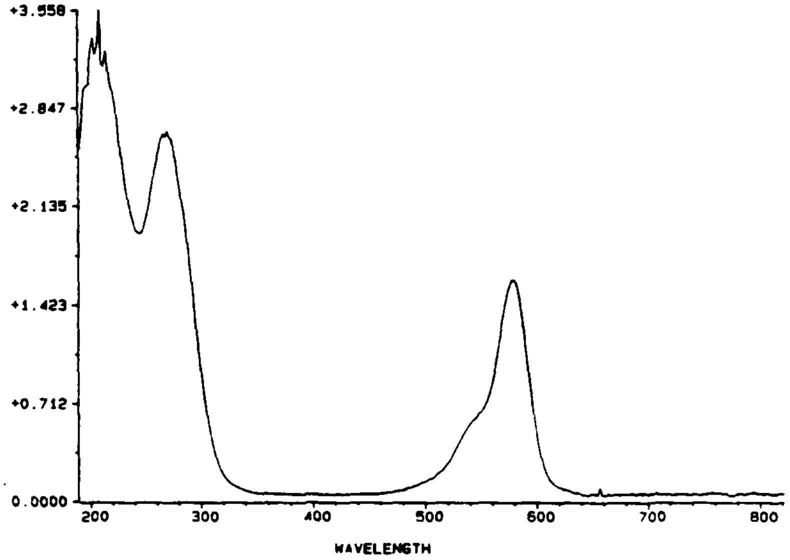

Figure 6-3: Absorbance of DODCI in Ethanol

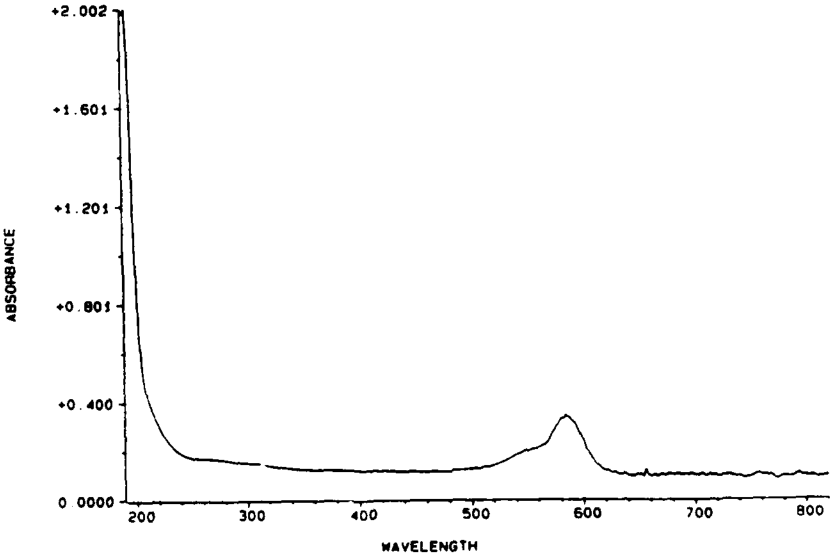

Figure 6-4: Absorbance of DODCI in Ethylene Glycol

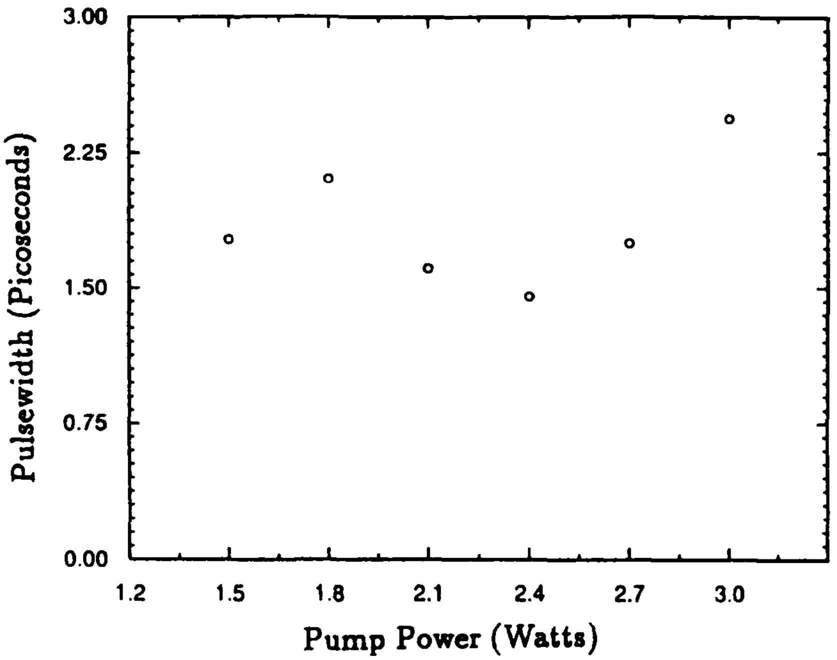

Figure 6-5: Hybrid Dye Laser Pulsewidth as a Function of Pump Laser Power at 576 Nanometers

to the red wavelengths, thus decreasing the effective cross-section of the saturable absorber from 3.65×01^{-16} cm^2 in ethanol to 2.1×10^{-16} cm^2 in ethylene glycol and lessening its effectiveness in pulse shaping. With this new σ_u^h, we can re-calculate the actual I_{sat} (using the same procedures as before) in the laser cavity to be 4.36×10^{12} $\frac{erg}{s-cm^2}$. Based on these calculations, we decided to vary the pump power to the hybrid dye laser system to determine the optimum pump power. Figure 6-5 on page 72 depicts the pulsewidth (on the $y - axis$) as a function of the pump laser power (on the $x - axis$) for the DODCI saturable absorber concentration set at 1.0×10^{-4} Molar.

We could not get the hybrid dye laser system to effectively lase at the 1.2 wattpump power, so trials at this level and lower were discontinued.

Based on these results, we then varied the DODCI saturable absorber concentration with various laser pump powers to determine the effect on the pulsewidth and shape. Figure 6-6 on page 73 depicts the pulsewidth (on the $y - axis$) as a function of the DODCI saturable absorber concentration (on the $x - axis$) for 1.8 watt pump power trial.

DODCI saturable absorber concentrations below $.75 \times 10^{-4}$ Molar were not at-

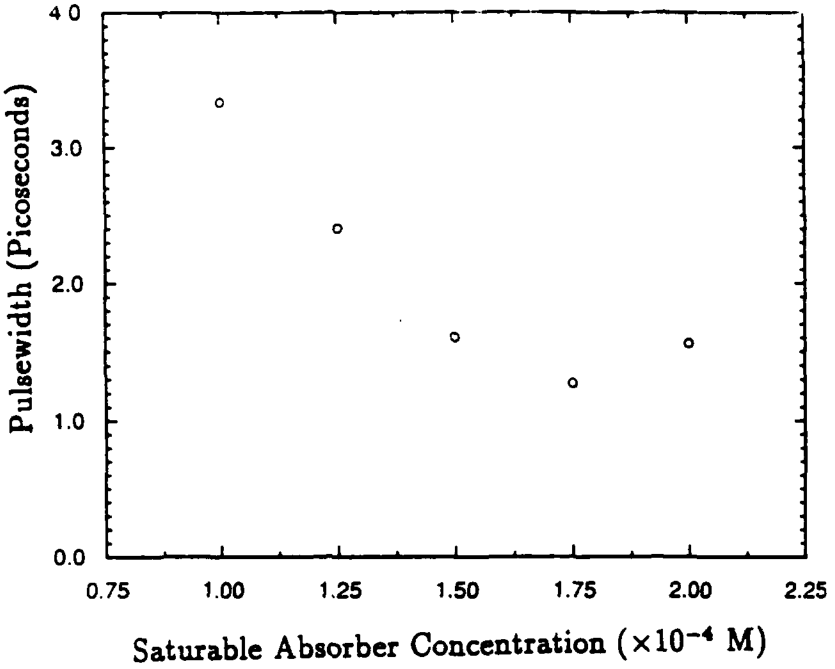

Figure 6-6: Hybrid Dye Laser Pulsewidth as a Function of DODCI Saturable Absorber Concentration at 576 Nanometers

tempted based on the inability of the saturable absorber jet to eliminate the background noise at this level. DODCI concentration levels above 2.0×10^{-4} Molar were not continued at the lower pumping levels as the output power of the laser was reduced in excess of 80 percent with no noticable decrease in pulsewidth or pulse shape. We were still not able to totally eliminate the incoherent background noise surrounding the coherence peak. The optimum performance that was achieved at the 576 nanometer wavelength is shown in figure 6-7 on page 74. The pump laser power was set at 1.5 watts and the DODCI saturable concentration was set 1.75×10^{-4} Molar. The resulting I_{in}^{peak} is calculted to be 7.13×10^{15} $\frac{erg}{s-cm^2}$ and the ratio, $\frac{I_{in}^{peak}}{I_{sat}}$, at this level was 1.6×10^{3}.

This system produced a real time pulsewidth of 1.16 picoseconds and average output power of 63 milliwatts. We were able to significantly reduce the incoherent background noise around the coherence peak, but were not able to eliminate it totally. This indicates that we were close to achieving optimal passive modelocking of the laser pulse in the laser cavity as indicated by the large $\frac{I_{in}^{peak}}{I_{sat}}$ ratio caused by the combination of the absorption cross section and dephasing time of DODCI at the 576 nanometer

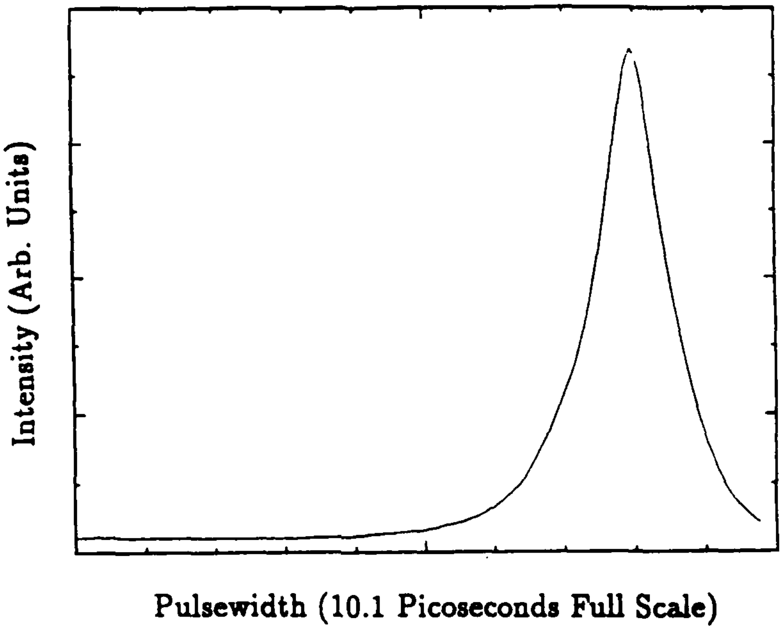

Figure 6-7: Optimum Hybrid Dye Laser Pulse at 576 Nanometers

wavelength.

The reason that we were not able to achieve a pulsewidth less than one picosecond turned out to be the group velocity dispersion (GVD) of the laser pulse. In picosecond and nanosecond regime laser pulses, the GVD does not effect the pulsewidth of the laser. As we approach the femtosecond regime, the sign of the GVD plays an important role in the pulse width and becomes the limiting factor as to how short of a pulse can be produced. A negative GVD is required to produce ultra-short lasers pulses in the femtosecond regime [Fork et al1983]. In a laser system with a positive GVD, the non-linear refractive mediums will broaden the pulse as the pulse tranverses the laser cavity. The second harmonic generation of the 532 nanometer wavelength pump pulse from LbO crystal of the Nd:YAG pump laser induces a positive GVD in the pump pulse [Shapiro1968]. Since the hybrid synchronous pumped dye laser uses this positive GVD pump pulse to create the dye pulse and the hybrid dye laser does not have a mechanism to compensate for or correct the GVD, the resulting dye pulse will also have a positive GVD. In the hybrid synchronous pumped dye laser cavity, the birefringent filter and the lasing and saturable absorber jet streams all function as non-linear refractive mediums and serve to further accentuate the broadening of the dye pulse and serve as a limiting factor to how short of a dye pulse can be produced.

To test this theory, we replaced the existing medium thickness birefringent filter of the hybrid dye laser with thinner birefringent filter with a thickness of 600 μm. By decreasing the pass length through the non-linear refractive medium that the laser pulse must transverse, we can reduce the amount of broadening caused by this effect. Initial trials with the thin BFR proved that this theory was correct. Another option to reduce the non-linear path length is to reduce the thickness of the dye and saturable absorber dye jets by "squeezing" the jet outlet to reduce the jet aperature size. Extreme care must be taken to ensure that the aperature shape is not deformed as this will adversely effect lasing operation. Since we now knew that the positive GVD of the dye laser would serve as a limiting factor to the pulsewidth, we decided to discontinue further trials at 576 nanometers and continue the experiment at the 556 nanometer wavelength.

Chapter 7

Experimental Results at 556 nanometer Wavelength

The second portion of the experiment involved using the hybrid synchronously pumped dye laser at the 556 nanometer wavelength required for the phase-interrupting collision experiment. The concentration of Rhodamine 6G dye in ethylene glycol was reduced to 2.5×10^4 Molar to achieve optimum performance at this wavelength. Since this 556 nanometer wavelength is at the edge of the Rhodamine 6G lasing dye curve, the standard Rhodamine 6G optics for the dye laser could not be used as the optics were not coated for reflection at peak efficiency at this wavelength. Instead, the appropriate high reflector mirrors in the laser cavity were replaced with Coumarin optics which are coated for peak reflection in this wavelength region. The initial results for the standard synchronous pumped dye laser without the saturable absorber produced an auto-correlated pulsewidth of 3.6 picoseconds with an average power of 160 milliwatts. We discovered the presence of the broad incoherent background surrounding the coherence spike of the pulse indicating that we were not properly passively modelocking the dye laser. We then attempted to correct this behavior through the use of the separate saturable absorber jet using DMETCI as the saturable absorber in the same manner as we did for DODCI at the 576 nanometer wavelength. The DMETCI saturable absorber was tried at various concentrations starting at the point $n\sigma_h^u l \sim 1$ with various pump laser powers to produce optimal pulse shapes, pulse widths and

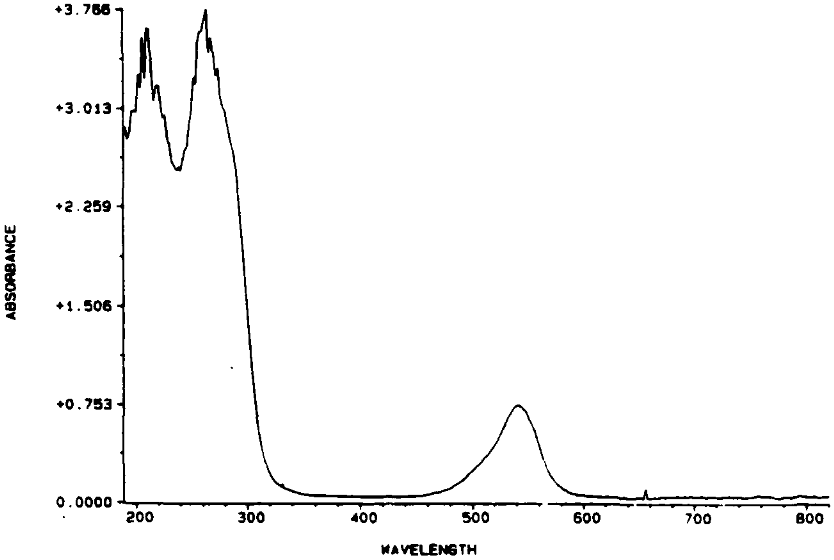

Figure 7-1: DMETCI Absorbance in Ethanol

output powers. The results are shown on the following pages.

First we tested the aborbance of DMETCI in ethylene glycol to determine how much red-shift was induced in the saturable absorber due to the different solvent. The absorbance chart on page 54 was based on DMSO as the saturable absorber solvent which is much less viscous than ethanol and ethylene glycol. The DMETCI saturable absorber dye absorbance in ethanol and ethylene glycol was tested since DMSO was not readily available using the ultra-violet / visible absorbance spectrometer to determine the amount of red-shift caused by the use of ethylene glycol in the saturable absorber dye jet. The results are shown in figure 7-1 for ethanol and figure 7-2 for ethylene glycol on page 77.

The absorbance of DMETCI is shifted less than DODCI when ethylene glycol was used as the solvent, but the relative absorbance at the 556 nanometer wavelength is not affected adversely. The resulting cross sections for DMETCI have been shifted from $1.54 \times 10^{-16}\ cm^2$ in DMSO to $1.58 \times 10^{-16}\ cm^2$ in ethanol to $1.60 \times 10^{-16}\ cm^2$ in ethylene glycol.

The results of the trials with DMETCI as the saturable absorber in the hybrid

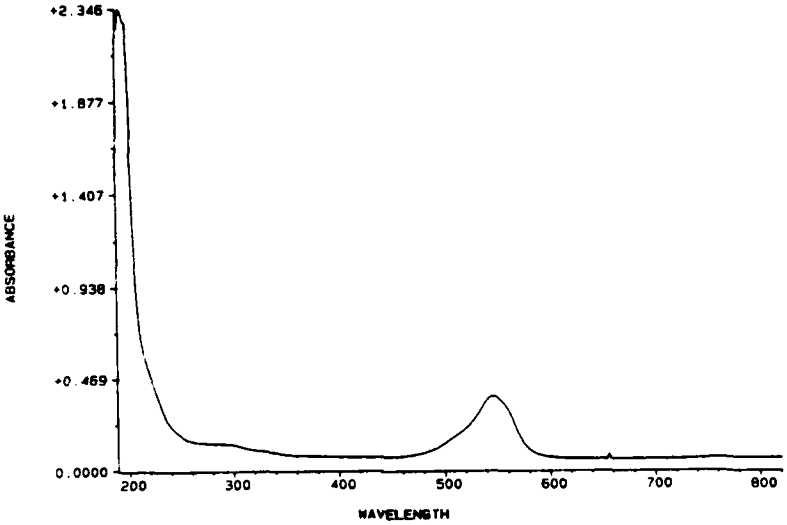

Figure 7-2: DMETCI Absorbance in Ethylene Glycol

synchronously pumped dye laser system is shown in the following figures.

Figure 7-3 on page 79 depicts the hybrid dye laser pulse width on the $y - axis$ as a function of the pump laser power on the $x - axis$. The DMETCI saturable absorber concentration was set at 1.5×10^{-4} Molar.

Again, the trials were stopped at 1.5 watts of pump laser power as we could not get the dye laser to effectively lase at this pumping level. Figure 7-4 on page 79 depicts the pulsewidth as a function of the DMETCI saturable absorber concentration for the optimum pumping power with the $x - axis$ now representing the laser output power. The pump laser power was set at 2.4 watts.

The limits on the saturable absorber concentrations were set in the same manner and under the same strictures as we did for the trials at the 576 nanometer wavelength. We also studied the pulsewidth and pulse shape as a function of the detuning of the laser cavity length as shown in figure 7-5 on page 80. The $y - axis$ represents the pulsewidth in units of picoseconds while the $x - axis$ represents the cavity detuning in micrometers. The point $x = 0$ represents the cavity detuning for the peak pulse amplitude and optimum pulse shape. The real-time pulse width at $x = 0$ is 1.01

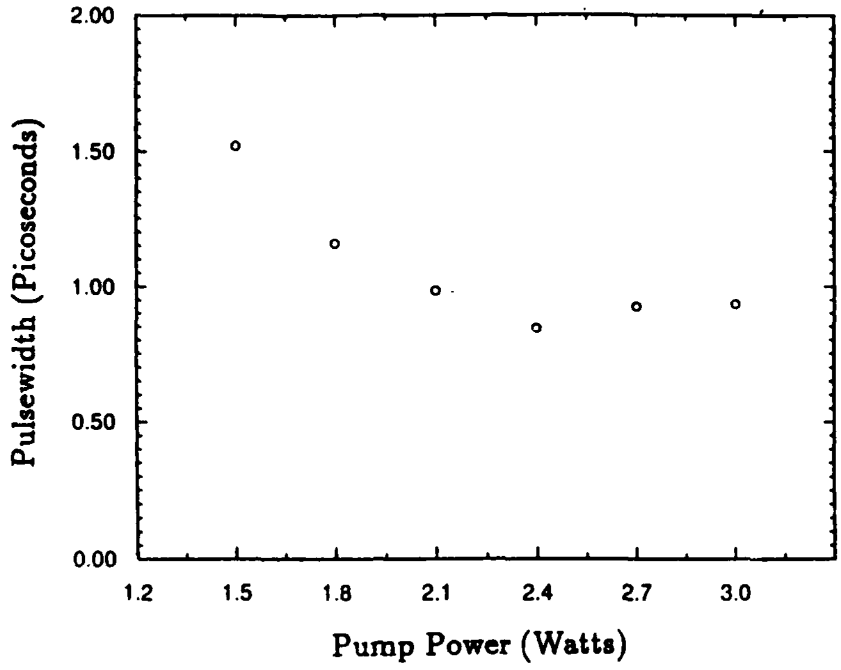

Figure 7-3: Hybrid Dye Laser Pulsewidth as a Function of Pumping Power with DMETCI Saturable Absorber at 556 nanometers

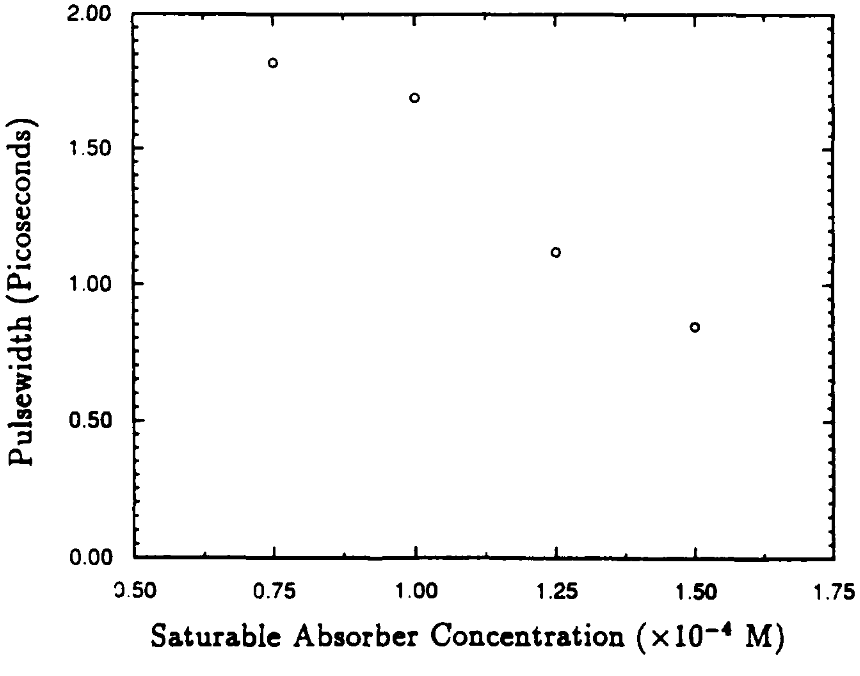

Figure 7-4: Hybrid Dye Laser Pulsewidth as a Function of DMETCI Saturable Absorber Concentration at 556 nanometers

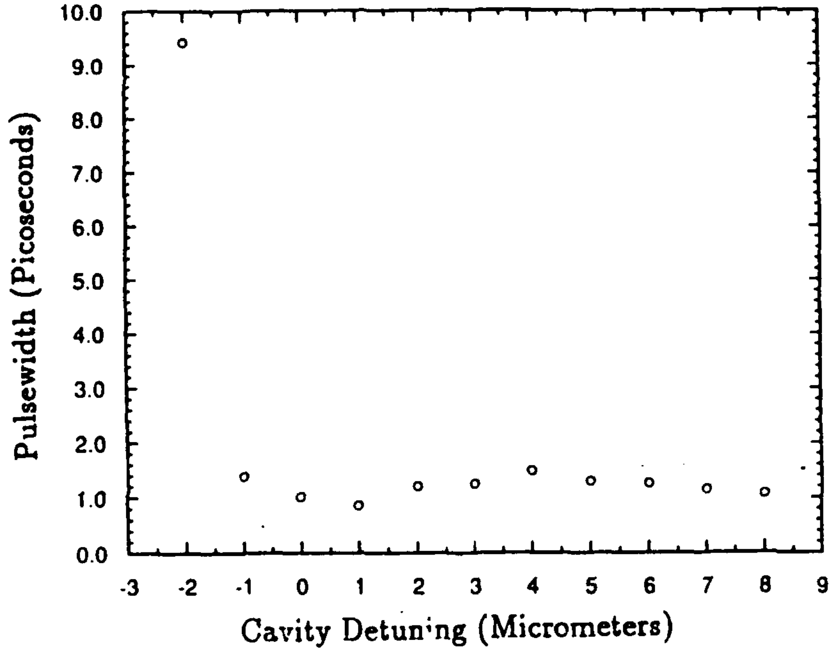

Figure 7-5: Hybrid Dye Laser Pulsewidth as a Function of Cavity Detuning at 556 nanometers

±10% picoseconds with the point with 1 μm of detuning produced a pulsewidth of 861 femtoseconds.

The optimal performance for DMETCI as the saturable absorber in the hybrid synchronously pumped dye laser is depicted in figure 7-6 on page 81. The saturable absorber dye concentration was set at 1.5×10^{-4} Molar while the Nd:YAG pump power was set as 2.4 Watts. The autocorrelated pulsewidth is 1.35 picoseconds and the average power is 31 milliwatts. The resulting real time pulsewidth was 823 femtoseconds.

We were able to totally eliminate the incoherent background noise and achieve a coherence peak that approached the theoretical hyperbolic $secant^2$ pulse shape. This indicated that we were properly passively mode-locking laser in accordance with the theory developed in Chapter 3.

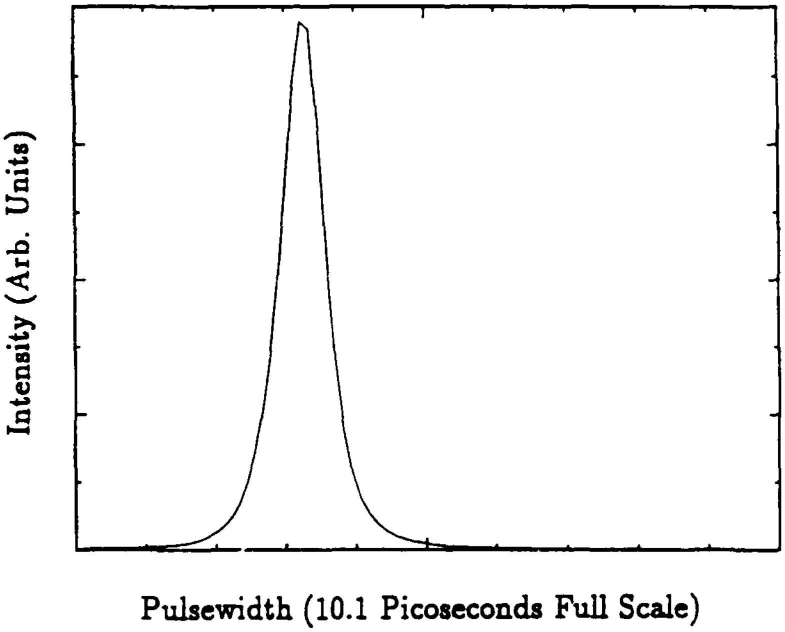

Figure 7-6: Optimum Rhodamine 6G Hybrid Dye Laser Pulse with DMETCI Saturable Absorber at 556 nanometers

Chapter 8

Analysis and Recommendations

In general, the experimental results are in general agreement with the theory and expected final output. We did achieve a sub-picosecond laser pulse with an increased power level over previous efforts that should prove to be effective in the phase-interrupting collision experiment.

8.1 Analysis

The experimental results are in general agreement with the theory. Figure 7-5 shows excellent agreement with the theory as the cavity mismatch parameter, Δ, must be less than 5 μm to achieve stable pulse shapes for the hybrid synchronous pumped laser. The tail of the detuning curve in this figure shows a decrease in the pulsewidth at detuning lengths beyond 4 μm. This is due to the development of the coherence peak from the "shoulders" of the pulse and shows a departure from the theoretical hyperbolic $secant^2$ pulse shape. The optimal hyperbolic $secant^2$ pulse shape could only be maintained for cavity detunings less than 2 μm. The shoulder of the pulse started to develop at the cavity detuning length of 3 μm and continued to develop until the cavity detuning length was 9 μm and the coherence peak disappeared. Figure 7-6 shows the optimal pulse shape and width for the 556 nanometer wavelength. We were able to totally eliminate the incoherent background noise and produce a pulse shape that approximates the theoretical hyperbolic $secant^2$ shape detailed in Chapter 3.

Experimental trials have shown that the best performance of the hybrid synchronous pumped laser output was at 556 nanometer wavelength and the output power was 31 milliwatts. Assuming this point to be the optimum ratio of cavity intensity to saturation intensity of the DMETCI saturable absorber jet, this figure can be used to develop an estimate of the dephasing time, T_2 for DMETCI. The power inside the cavity is therefore $P_{in} = \frac{P_{out}}{Transmission}$. The transmission of the output coupler is given at 5 percent by factory specification which gives a P_{in} equal to 620 mW. The P_{in}^{peak} equals the P_{in} divided by the duration of the pulse before the saturable absorber effects, $\tau_{pulse} = 3.625$ ps, divided by the number of pulses per second, 76 Mhz. This yields a $P_{in}^{peak} = 2.25 \times 10^3$ W.

The spot size on the high reflector mirror from the Coherent specifications is $2\omega_0 = .05 \pm .01$ cm. The focus, f, of the high reflector mirror is 2.5 cm. The beam waist on the saturable absorber jet is given by

$$\omega = \frac{\lambda f}{\pi \omega_0} \tag{8.1}$$

which yields a beam waist, ω, equal to 1.77×10^{-3} cm. The peak intensity, I_{in}^{peak}, inside the saturable absorber jet then becomes

$$I_{in}^{peak} = \frac{P_{in}^{peak}}{\pi \omega^2} \tag{8.2}$$

or $I_{in}^{peak} = 2.29 \times 10^8 \frac{W}{cm^2}$ or $2.29 \times 10^{15} \frac{erg}{s-cm^2}$. We now need to calculate the σ_h^u for DMETCI from the absorbance chart for ethylene glycol. Using the figures for the appropriate dye concentration, the path length through the dye jet, and the ϵ value from figure 7-2 yields a $\sigma_h^u = 1.6 \times 10^{-16}\ cm^2$. The ratio, $\frac{I_{in}^{peak}}{I_{sat}} = 1.6 \times 10^3$ in Chapter 7 for the 576 nanometer wavelength produced a pulse that consisted of a coherence peak above the low incoherent background noise. If we assume a ratio of one half of theis value (on the order of $.8 \times 10^3$) for the 556 nanometer wavelength sample since we eliminated the background, we can approximate the I_{sat} for DMETCI as $2.86 \times 10^{12} \frac{erg}{s-cm^2}$. This means that the T_2 for DMETCI from equation 3.1 is then

$$T_2 = \frac{\hbar c}{2\sigma_h^u \lambda I_{in}^{peak}} \tag{8.3}$$

This gives an estimated value of for T_2 equal to 621 picoseconds as compared to the previously estimated value of 250 picoseconds. Some factors leading to this discrepancy include the variation in spot size measurement for the calculation of the incident intensity, an incorrect assumption of the relationship between I_{in}^{peak} and I_{sat} for proper passive modelocking and the variation in power output from the dye laser resulting from the pump laser variation or improper internal alignment of the hybrid dye laser optics.

The primary reason that we did not achieve more favorable results in creating shorter pulsewidths is that we were limited in the pulse width generation by the positive group velocity dispersion of the laser system. Non-linear refractive mediums in the laser cavity such as the saturable absorber and laser dye jets and the quartz crystal used in the birefringent filter for laser frequency tuning tend to exacerbate the positive GVD of the laser by increasing the pulse width in frequency as it transverses the non-linear medium. Theoretical and experimental evidence has shown the requirement for a negative GVD in ultra-short pulse generation [R.L. Fork et al1983]. The current laser system does not have the capability to compensate for the positive GVD to decrease the GVD and resulting pulsewidth.

Another reason that this experiment did not reach the theoretical limits of the hybrid synchronously pumped laser is that we were not able to effectively maintain the cavity tuning factor, Δ, the difference of the cavity length of the dye laser from the cavity length of the pump laser. The theory section of this thesis demonstrates that optimum mode-locking and power output occurs when the cavity mis-match is within 5 micrometers. Equation 3.26 shows the direct relation between the cavity mismatch Δ and the achievable full-width half maximum pulsewidth as $t_p = \frac{3.5\Delta}{ln(R_l G_0)}$. Fluctuations in the dye jet thickness for the lasing dye medium and saturable absorber caused by possible contaminants in the dyes and solvents and fluctuations in the pumping pressure all contribute to the random variation in the cavity mismatch Δ

above and beyond the simple geometrical variation in cavity length. This factor is beyond the capability of outside control.

Stability of the pump laser output also contributed to the limitations of experimental results. Although we were able to maintain laser output power fluctuations to under 5 percent, this random fluctuation still contributed to the variations in pulse shape. Chapter 3 clearly points out the relationship between the pump laser pulse and the resulting dye laser pulse. The majority of the calculations for the steady state laser gain equations and dye laser pulse shape assume a slowly varying gain and pump pulse over the duration of the dye pulse formation and development. Larger variations in the pump power and gain medium limit the validity of the assumptions used in deriving these equations .

Other factors contributing to the limits were the availability and use of the proper laser optics for the various mirror assemblies in the laser cavity. Where possible, we tried to use optics that were coated and designed for the laser and wavelength that we were operating at. This was not possible in all cases, especially in the case of the 556 nanometer wavelength since the required optics were not commercially available for this laser arrangement at this wavelength.

8.2 Recommendations

Based on the results of this experiment, this laser system should use the Hybrid synchronously pumped laser system with Rhodamine 6G as the lasing dye at 2.49×10^{-4} Molar Concentration with DMETCI as the saturable absorber at 1.5×10^{-4} Molar concentration. The dye laser system should be pumped with the Nd:YAG output of 2.4 Watts. This hybrid laser system produced as optimal shaped pulsewidth of 823 femtoseconds with an output power of 31 milliwatts. The satellite pulses and broad incoherent background from the laser pulse output of the original laser system have been eliminated, resulting in a clear hyperbolic *secant*^{2} pulse shape. These final laser parameters should allow sufficient resolution of the details of the phase-interrupting collision experiment to be discerned.

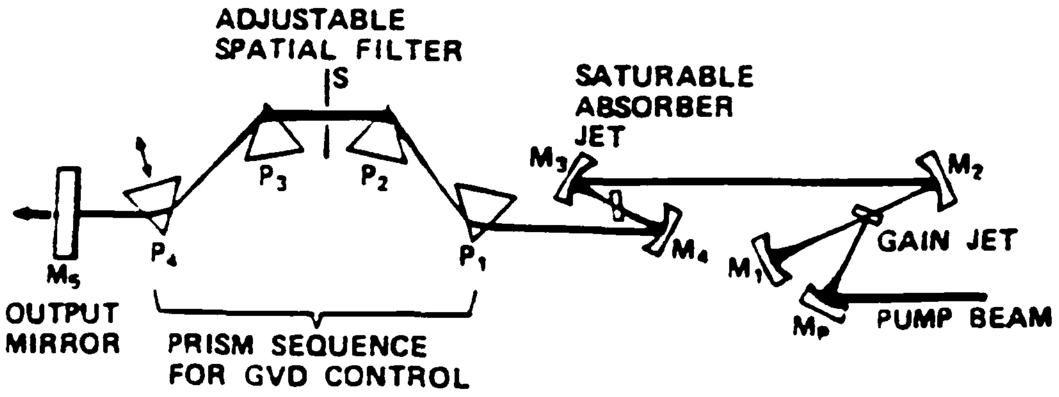

Figure 8-1: Hybrid Synchronous Pumped Dye Laser with GVD Compensation [Nakazawa et al1987]

An option to further decrease the pulsewidth of the existing system is the addition of a four prism system to compensate for the positive group velocity dispersion of the laser pulse. This system was developed by R.L Fork [R.L Fork et al1983] to compensate for positive GVD without changing the laser beam path and further refined for the Rhodamine 6G dye by M. Nakazawa [Nakazawa et al1987] This method uses four prisms sets at Brewster's angle to minimize losses and can decrease the pulsewidth without further decrementing the output power. The apparatus is set up as in integral part of the laser cavity and is depicted in figure 8-1.

The amount of GVD compensation is controlled by the translation of the fourth prism in the laser beam path. As the path length through the quartz prism increases, the GVD of the laser cavity decreases. The four prism GVD compensation system will require the purchase of four prisms coated with an anti-reflective coating peaked near 556 nanometers with each prism mounted separately on a 360 degree rotational stage and each rotational stage mounted on an XYZ translation stage. The positioning of the hybrid dye laser components will have to be altered to include the four prism system within the cavity length of the laser. If the hybrid laser system with GVD compensation still cannot produce a sufficiently short pulse with adequate output power for the phase-interrupting collision experiment, an alternative option for optimum performance and power at the 556 nanometer wavelength is the purchase of a third harmonic generator for the Antares 76-S Nd:YAG laser that will enable the use of Rhodamine 110 laser dye in the hybrid synchronously pumped laser at 556 nanometer wavelength. This dye has a peak fluorescence of 562 nanometers when pumped with the third harmonic Nd:YAG laser. This combination should produce maximum power output and pulse shape for the experiment as we will be operating in the maximum efficient region of the laser dye. If a sufficiently short pulsewidth is still not achieved by the hybrid synchronously pumped dye laser, this third harmonic generator with Rhodamine 110 system produces enough power to allow for the use of the external pulse compression apparatus and still achieve sufficient power at the sample cell to produce viable results for the phase-interrupting collision experiment.

Appendix A

Hybrid Synchronous Pumped Dye Laser Gain Equation

A.1 General Laser Gain Equation

In this appendix, the complete laser gain equation for the hybrid synchronous pumped dye laser is outlined from the initial pass of the pump pulse through the lasing dye jet through the requirement for the inclusion of the spontaneous emission effects into the steady state gain equation. On the first pass through the dye jet, the dye pulse, $I(\tau)$, experiences a gain

$$I_1(\tau) = G_1(\tau)I(\tau) \tag{A.1}$$

and satisfies the gain equation

$$\frac{dG_1}{d\tau} + \sigma G_1[I(\tau)(G_1 - 1) - I_p(\tau)] = 0 \tag{A.2}$$

where $I_p(\tau)$ corresponds to the pump pulse. The dye pulse then transverses the cavity, strikes the end mirror and returns through the dye jet again where it experiences the gain

$$I_2(\tau) = G_2(\tau)I_1(\tau) = G_1(\tau)G_2(\tau)I(\tau) \tag{A.3}$$

The pump pulse is assumed to have exited the dye jet by the time the dye pulse returns to the dye jet for and the gain equation for the second passage through the dye jet becomes

$$\frac{dG_2}{d\tau} + \sigma G_2 I_1(\tau)(G_2 - 1) = 0 \tag{A.4}$$

Defining

$$G(\tau) = G_1(\tau)G_2(\tau) \tag{A.5}$$

and taking the derivative with respect to τ, we can combine the two gain equations for the two passes into the general form gain equation

$$\frac{dG}{d\tau} + \sigma G[I(\tau)(G-1) - I_p(\tau)] = 0. \tag{A.6}$$

A.2 Initial Dye Pulse Gain Equation

Defining τ_0 as the time the dye pulse is generated from the pump laser pulse striking the dye jet, the dye pulse in the laser cavity can be essentially neglected for $\tau \leq \tau_0$ and the round trip total gain takes the form

$$G(\tau) = G_2(\tau_0)G_1(\tau) \tag{A.7}$$

and describes the rise of the gain from the ground state absorption level caused by the pump pulse. We define the ground state absorption level, G_0, as

$$G_o = e^{-\sigma_a n_T d} \tag{A.8}$$

where σ_a is the absorption cross-section of the lasing dye at dye laser wavelength λ, n_T is the number of lasing dye molecules per cubic centimeter in the dye stream, and d is the distance through the dye jet that the pump pulse transverses. Under this definition, $G_1(\tau)$ is the solution of equation A.7 with initial conditions, $I = 0$ and $G = G_o$ and has the form

$$G_1(\tau) = G_o e^{\sigma \int_{-\infty}^{\tau} I_p(t)dt} \tag{A.9}$$

Defining

$$E_p(\tau) = \int_{-\infty}^{\tau} I_p(t)dt \tag{A.10}$$

and

$$X_p(\tau) = e^{\sigma E_p(\tau)} \tag{A.11}$$

this can be more simply written as

$$G_1(\tau) = G_o X_p(\tau) \tag{A.12}$$

For $\tau_0 \leq \tau$, the total gain, $G(\tau_0)$ is equal to the product of the round trip gains $G_1(\tau)$ from equation A.12 and $G_2(\tau_0)$ where $G_2(\tau_0)$ is equal to [Yasa1983]

$$G_2(\tau_0) = G_o[\frac{XX_p}{1 + G_1(\tau_0)(X-1)}]^{\gamma} \tag{A.13}$$

where

$$\gamma = e^{-T_m/T_2} \tag{A.14}$$

where T_m is the round trip travel time from the dye jet to the output mirror, and T_2 is the fluorescence lifetime of the lasing dye and

$$X = e^{\sigma E(\tau=\infty)} \tag{A.15}$$

$$X_p = e^{\sigma E_p(\tau=\infty)} \tag{A.16}$$

and

$$E(\tau) = \int_{-\infty}^{\tau} I(t)dt \tag{A.17}$$

The arguments, equations A.14, A.15, A.16, and A.17 of equation A.13, account for the minimal fluorescence remaining in the laser dye molecules from the initial gain passage, $G_1(\tau)$, of the pulse at τ_0 as it initially transited the lasing dye jet.

A.3 Spontaneous Emission Effects

For times after τ_0, the pump pulse can essentially be neglected in the dye pulse region because the intensity of the pump pulse becomes much less than the dye pulse intensity ($I_p \ll I$). I_p can essentially be neglected in terms of the dye pulse, and the solution to equation A.2 becomes

$$G(\tau) = \frac{G(\tau_0)X(\tau)}{1 + G(\tau_0)(X(\tau) - 1)} \tag{A.18}$$

A dye laser pulse starting with an intensity, $I(\tau)$, will experience a gain, $G(\tau)$, and a linear cavity loss, R_l, and produce a final output intensity, I_f, after one full trip of

$$I_f(\tau) = R_l G(\tau) I(\tau) \tag{A.19}$$

For differing pump laser cavity lengths and dye laser cavity lengths, there will be a mismatch parameter,

$$\Delta = \frac{L - L_p}{c} \tag{A.20}$$

where L is the dye laser cavity length and L_p is the pump laser cavity length, causing the pump and dye pulses to arrive at differing times at the lasing dye jet. Equation A.19 then becomes

$$I_f(\tau + \Delta) = R_l G(\tau) I(\tau) \tag{A.21}$$

It turns out that the spontaneous emission effects of the laser dye medium cannot be neglected in the steady state condition. Without spontaneous emission, equation A.21 is a solution for equation A.2 over a single round trip. As the number of round trips increases, a stabilized dye pulse cannot be sustained in the cavity for a given Δ since the forward edge of the pulse will always experience greater cavity losses in the region for $\Delta > 0$ that will inhibit a steady state condition [Herrmann1982]. Therefore, the evolution of the pulse must take spontaneous emission effects into consideration in the rate equations. In section A.2 where $\tau < \tau_0$, the dye pulse has minimal effect on the excited state population of the laser dye molecules in the dye stream. Neglecting ground state dye absorption from the returning dye pulse, the interaction within the dye stream is governed by the following set of equations

$$(\frac{\partial}{\partial x} + \frac{1}{c}\frac{\partial}{\partial t})I = \sigma n_1(I + I_p) \tag{A.22}$$

$$(\frac{\partial}{\partial x} + \frac{1}{c}\frac{\partial}{\partial t})I_p = -\sigma_p n_0 I_p \tag{A.23}$$

$$\frac{dn_o}{dt} = -n_0 \sigma_p I_p \tag{A.24}$$

$$n_0 + n_1 = n_T \tag{A.25}$$

where I_{sp} is the intensity of the spontaneous emission into a solid angle subtended by the dye beam [Yasa1983]. When the dye pulse exits the dye jet, its intensity, $I(\tau)$, will satisfy the one pass gain equation A.1 .

$$I(\tau) + I_{sp} = [I_0(\tau) + I_{sp}]G_0(\tau) \tag{A.26}$$

where $I_0(\tau)$ is the initial gain intensity at the face of the dye jet and

$$G_0(\tau) \simeq e^{\sigma \int_{-\infty}^{\tau} I_p(t)dt} \tag{A.27}$$

For two passages of the dye jet on the first round trip by the dye pulse, the final pulse output of the first pass is used as the input pulse of the second pass and there is no I_p for the second pass (an initial assumption in section 3.2.1), the final pulse of the full round trip becomes

$$I_1(\tau) = R_l G(\tau) I_0(\tau - \Delta) + I_{sp}[G(\tau) - 1] \tag{A.28}$$

The second round trip produces

$$I_2(\tau) = R_l^2 G(\tau) G(\tau - \Delta) I_0(\tau - 2\Delta) + I_{sp}[R_l G(\tau) G(\tau - \Delta) + G(\tau)(1 - R_l) - 1] \tag{A.29}$$

for n round trips, the resultant $I_n(t)$ is

$$I_n(t) = R^n l G(\tau) G(\tau - \Delta) ... G(\tau - (n-1)\Delta) I_0(\tau - n\Delta) + I_n^{sp}(\tau) \tag{A.30}$$

where $I_n^{sp}(\tau)$ is [Yasa1983]

$$\begin{aligned} I_{n+1}^{sp} = I_{sp}[R_l^n G(\tau) G(\tau - \Delta) \ldots G(\tau - n\Delta) + R_l^{n-1} \\ *(1 - R_l) G(\tau) G(\tau - \Delta) \ldots G(\tau - (n-1)\Delta) \\ + \ldots + R_l^p G(\tau - p\Delta) \ldots G(\tau - \Delta) G(\tau)(1 - R_l) + \ldots \\ + R_l G(\tau - \Delta) G(\tau)(1 - R_l) - 1] \end{aligned} \tag{A.31}$$

For a large number n round trips, the magnitude of the first term of $I_n(\tau)$ essentially vanishes with respect to the other terms and $I_n(\tau)$ approaches I_n^{sp}. This demonstrates that the pump pulse dies out after several passes through the dye laser cavity, and the dye laser pulse intensity depends on the spontaneous emission effects. I_{n+1}^{sp} and I_n^{sp} can be reduced to

$$I_{n+1}^{sp}(\tau) = I_{sp}[R_l^n G(\tau) G(\tau - n\Delta) + (1 - R_l) R_l^{n-1} G(\tau) \ldots G(\tau - (n+1)\Delta)] + Oterms \tag{A.32}$$

$$I_n^{sp}(\tau) = I_{sp}[R_l^n G(\tau)G(\tau - \Delta)\dots G(\tau(n-1)\Delta)] + Oterms \tag{A.33}$$

Expressing I_{n+1}^{sp} in terms of I_n^{sp} gives

$$I_{n+1}^{sp}(\tau) = I_{sp}R_l^n G(\tau)G(\tau - \Delta)\dots G(\tau - (n+1)\Delta)[G(\tau - n\Delta) - 1] + I_n^{sp}(\tau) \tag{A.34}$$

For $\tau \ll n\Delta$, the first term in I_{n+1}^{sp} goes to zero and we get the resultant

$$I_{n+1}^{sp} = I_n^{sp} \tag{A.35}$$

This implies that for a sufficient number of trips through the dye laser cavity that the evolved laser intensity will reach a steady state condition with a conserved pulse shape. Equation A.28 becomes

$$I(\tau) = R_l G(\tau)I(\tau - \Delta) + I_{sp}[G(\tau) - 1] \tag{A.36}$$

In this equation, the $G(\tau)$ is considered independent of the dye laser intensity in the region $\tau \leq \tau_0$. In equation A.31 , $R_l G(\tau \leq 0) = 1$ and $I(\tau) = I_{sp}(\tau)$. In the region defined by $\tau \geq \tau_0$, $I(\tau)$ increases with τ and affects $G(\tau)$. Equation A.31 then converges to a value $I(0) \gg I_{sp}$, demonstrating that the spontaneous emission-evolved dye laser intensity builds up in an ultra-short time period. Over a sufficient number of round trips through the cavity for $\tau \geq 0$, the steady state conserved pulse shape is achieved and the spontaneous emission effects for the round trip can be neglected [Yasa1983]. The spontaneous emission effects essentially shift the dye pulse forward to offset the increased retardation due to the cavity mismatch, Δ. As Δ increases, the stability of the conserved pulse shape dramatically decreases and the resulting pulsewidth dramitically increases.

Appendix B

Data Analysis Programs

The following programs, "Autoco.c" and "Analize.it" were written by Kyunwon An and were used to analyze the data taken during the experiment.

"Analize.it" takes the autocorrelated pulse data from "Autoco.c", normalizes the data for the solenoid travel range and produces the output seen in this thesis for the pulse shapes.

analize.it Fri May 31 01:04:51 1991

```
#! /usr/bin/csh
# $1-asyst file
# $2-print flag, '-p'

# first extract envelop data
xanalysis -r4 $1

# remove tmpfile if exists
rm -f tmpfile

# put together envelops into a single file
echo 'putting together envelop data as tmpfile'
column -m11 <$1.low1 >tmpfile
column -m11 -o1256 <$1.up1 >>tmpfile
column -m11 -o1512 <$1.low2 >>tmpfile
column -m11 -o1768 <$1.up2 >>tmpfile

# output
echo 'rescaling tmpfile and saving it as' $1.scaled
# remove $1.scaled if exists
rm -f $1.scaled

autoco <tmpfile |column -m011 > $1.scaled

if ($2 == '-p') then
echo 'generating a postscript image on printer'
xyplot $1.scaled -y1-2048 -y20 -x1-0.5 -x20.5 -xu0.5 -xt5 -Lautoco.label -sm -p -sf |lpr
 -h
lpq
else
xyplot $1.scaled -y1-2048 -y20 -x1-0.5 -x20.5 -xu0.5 -xt5 -Lautoco.label -sm -sf
endif

# clean up
rm $1.up1 $1.low1 $1.up2 $1.low2
rm tmpfile
```

"Autoco.c" compensates for the motion of the solenoid and produces the autocorrelated pulse envelop.

```
autoco.c        Fri May 31 13:34:35 1991

#include        <stdio.h>
#include        <math.h>
#define PI              3.14159265
#define max_n_local     20
#define label_file      "autoco.label"
#define aux_file        "autoco.aux"

double  _t12, _T;

double  displacement(t)
double  t;
{
return 0.5*cos((t-_t12)/_T*2.*PI);
}

main()
{
double  t[1024], s[1024], s_local[max_n_local];
struct triplet {
        int     begin, center, end;
        };
struct triplet  index[max_n_local];
FILE    *stream;

int     i, j, n, was_inside, j_min, i_start, i_stop, i_max, i_min;
double  s_min, s_max, s_trigger, dT;

/* open aux_file for record */
stream = fopen(aux_file, "w");

/* read raw signal */
i = 0;
while (scanf("%lf %lf", &t[i], &s[i])!=EOF) ++i;
n = i;

/* find global minimum & maximum */
s_min = 2048.;
s_max = -2048.;
for (i=0; i<n; ++i) {
        if (s_min > s[i]) {
                s_min = s[i];
                i_min = i;
                }
        if (s_max < s[i]) {
                s_max = s[i];
                i_max = i;
                }
        }
fprintf(stream, "global maximum: %.3lf at i=%d\n", s_max, i_max);
fprintf(stream, "global minimum: %.3lf at i=%d\n", s_min, i_min);

/* set trigger level at 50 % */
s_trigger = 0.5*(s_min+s_max);

/* third find three local minima */
for (i=0; i<max_n_local; ++i) s_local[i] = 2048.;
was_inside = 0;
j = 0;
j_min = 0;

for (i=0; i<n; ++i) {
        if (s[i] < s_trigger) {
                if (!was_inside) {
                        was_inside = 1;
```

```
                        index[j].begin = i;
                        }
                if (s_local[j] > s[i]) {
                        s_local[j] = s[i];
                        index[j].center = i;
                        if (s[i] == s_min) j_min = j;
                        }
                }
        else {
                if (was_inside) {
                        was_inside = 0;
                        index[j].end = i;
                        ++j;
                        }
                }
        }

/* if j<3 then data cannot be analized */
if (j<3) {
        fprintf(stderr, "Error: number of local minima is less than 3\n");
        exit();
        }

/* otherwise go on */
fprintf(stream, "There are %d local minima found:\n", j);
for (i=0; i<j; ++i)
        fprintf(stream, "%.3lf at i=%d\n", s_local[i], index[i].center);
fprintf(stream, "The pulse #%d is the largest\n", j_min+1);

/* set global variables for function displacement */
_t12 = (t[(index[0].center)] + t[(index[1].center)])/2.;
_T = t[(index[2].center)] - t[(index[0].center)];

fprintf(stream, "t12=%.3lf T=%.3lf\n", _t12, _T);

/* output of largest pulse */
i_start = 0;
i_stop = n;

if (j_min>0) i_start = (index[j_min-1].center + index[j_min].center)/2;
if (j_min<j-1) i_stop = (index[j_min].center + index[j_min+1].center)/2;

fprintf(stream, "output is written from i=%d to i=%d\n", i_start, i_stop);
fclose(stream);

for (i=i_start; i<i_stop; ++i)
        printf("%lf %lf %lf\n", t[i], displacement(t[i]), s[i]);

/* make label file for xyplot */
stream=fopen(label_file, "w");
fprintf(stream, "normalize time\n");
fprintf(stream, "auto-correlation\n");
dT=fabs(displacement(t[index[j_min].begin])
        - displacement(t[index[j_min].end]));
fprintf(stream, "The pulse width(FWHM) is %.3le in normalized unit.\n", dT);
fclose(stream);
}
```

Bibliography

[An et al1988] Kyungwon An, R.R. Dasari, J.E. Thomas and M.S. Feld, "Time Domain Study on decay of Atomic Superposition States due to Phase-interrupting Collisions", George H. Harrison Spectroscopy Laboratory Annual Report MIT (1988).

[Catherall et al1982] J.M. Catherall, G.H.C. New and P.M. Radmore, " Approach to the theory of mode-locking by synchronously pumping dye lasers", Optical Letters 7, 319 (1982)

[Corliss1962] C.H. Corliss and W.R. Bozman, "Wavelengths, Energy-Levels, Transition Probabilities and Oscillator Strengths of 70 Elements" (USNBS # 53, 1962).

[Couillaud1985] B. Couillaud and V. Fossati-Bellani, "Mode-Locked Lasers and Ultra-Short Pulses", Lasers and Applications, Feb (1985).

[Feld1977] M.S. Feld, "Frontiers in Laser Spectroscopy", North Holland Publishing Co. 1977.

[Fleming1986] G. Fleming, "Chemical Applications of Ultrafast Spectroscopy", Oxford University Press, 1986.

[Forber1983] Richard Alan Forber, "Fundamental Studies of Collisional Processes in the First Resonance Transition of Ytterbrium", Phd Thesis, MIT, 1983.

[Fork et al1983] R.L. Fork, C.V. Shank, R.Yen and C.A. Hirlimann, "Femtosecond Optical Pulses", IEEE Journal of Quantum Electronics, QE-19, 500 (1983)

[Fork et al1984] R.L. Fork, O.E. Martinez and J.P. Gordon, " Negative Dispersion using pairs of prisms", Optics Letters, Vol 9. No. 5 May (1984).

[Frantz1963] L.M. Frantz and J.S. Nodvik, "Theory of pulse propagation in a laser amplifier", Journal of Applied Physics, Vol. 34 (1963).

[Frigo1983] N.J. Frigo, "Ultrashort Pulse Generation in Saturable Media: A Simple Physical Model", IEEE Journal of Quantum Electronics, Vol. QE-19, No. 4, Apr (1983).

[Ghosh1985] A.P. Ghosh, "Isolated Multipole Echoes and Multipole Velocity Changing Collision Kernels in Yb^{174}", Phd Thesis, MIT 1985.

[Ghosh et al1984] A.P. Ghosh, C.D. Nabors, M.A. Attili, J.E. Thomas and M.S. Feld, "Laser Polarization Transients to Study Non-Classical Features of Magnetic Quantum States in $Ytterbrium^{174}$", Physical Review Letters 53 Vol 14 Oct (1984).

[Grischkowsky1983] D. Grischkowsky and A.C. Balant, "Optical Pulse Compression based on Enhanced Frequency Chirping", Applied Physics Letters 41, Jun (1983).

[Hansch1969] T.W. Hansch and P. Toschek, "On pressure broadening in a He-Ne Laser" IEEE Journal of Quantum Electronics 5, 61 (1979).

[Herrmann1982] J. Herrmann and U. Motschmann, "Theeory of the Synchronously Pumped Picosecond Dye Laser" Applied Physics B, No. 1, 27 (1982).

[Kaiser1988] W. Kaiser ed., "Topics in Applied Physics - Ultra-Short Laser Pulses and Applications", Vol 60, Springer-Verlag Co, 1988.

[Lambda1986] Ulrich Brackman, "Lambdachrome Laser Dyes", Lambda Physik GmbH, 1986.

[Le Gouet1980] J.L. Le Gouet and R. Vetter, "Depolarizing Collisions in a three-level system of Xe I" Journal of Physics B, 13, L147 (1980).

[Michaelson1885] A.A. Michaelson, AstroPhysics Journal 2, (1885).

[Nakazawa et al1987] M. Nakazawa, T. Nakshima, H. Kubota and S. Seikai, "65 femtosecond Pulse Generation from a Synchronously pumped Dye Laser without a Colliding Pulse Mode-Locking Technique" Optics Letters, Vol 12, No 9 681 (1987).

[Nesmeyanov1963] A.N. Nesmeyanov, "Vapor Pressure of the Chemical Elements", Elsevier Publishing Company, NY 1963.

[New1972] G.H.C. New, "Mode-Locking of quasi-continous lasers", Optical Communications, Vol. 6, (1962).

[New1974] G.H.C. New, "Pulse evolution in mode-locked quasi-continous lasers", IEEE Journal of Quantum Electronics, Vol. QE-10, Feb, (1974).

[Pinard1979] M.Pinard, C.G. Aminoff and F. Laloë, "Velocity-Selective Optical

Pumping and Doppler-Free Spectroscopy", Physical Review A, June (1979).

[Rebane1967] V.N. Rebane "The Effect of Collisions on the Polariaztion of Resonance Fluorescence", Optical Spectroscopy, (1967).

[Ruilliere1976] C. Ruilliere, "", Chemistry Physical Letters, 43(2) 303 (1976).

[Ryan et al1978] J.P. Ryan, L.S. Goldberg and D.J. Bradley "Comparison of Synchronous Pumping and Passive Mode-Locking of CW Dye Lasers for the Generation of Picosecond and SubPicosecond Light Pulses", Optics Communications Vol 27 No.1, Octo (1978).

[Shapiro1968] S.L. Shapiro, "Second Harmonic Generation in $LiNbO_3$ by Picosecond Pulses", Applied Physics Letters, 13, 19 (1968).

[Sibbett1982] W. Sibbett and J.R. Taylor, "", Optical Communications, 43 (1) 50 (1982).

[Tomlinson1984] W.J. Tomlinson, R.H. Stolen and C.V. Shank "Compression of Optical Pulses chirped by self-phase modulation in fibers", Journal of the Optical Society of America B, Apr, (1984).

[Watanabe et al1983] A. Watanabe, H. Takemura, S. Tanaka, H. Kobayashi, and M. Hara, "Compression Mechanism of Subpicosecond Pulses by Malachite Green Dye in Passively Mode-Locked Rhodamine 6G/ DODCI CW Dye Lasers", IEEE Journal of Quantum Electronics, Vol. QE-19, No. 4, Apr (1983).

[Yasa1975] Z.A. Yasa and O. Teschke, Optical Communications, 15, 169 (1975)

[Yasa1983] Z.A. Yasa, "Theory of Synchronously Pumped Dye Lasers", Applied Physics B 30 (1983).